Atmos. Meas. Tech. Discuss., 3, 4009–4057, 2010
www.atmos-meas-tech-discuss.net/3/4009/2010/
doi:10.5194/amtd-3-4009-2010

Atmospheric Measurement Techniques Discussions

Retrieval of water vapor vertical distributions in the upper troposphere and the lower stratosphere from SCIAMACHY limb measurements

A. Rozanov[1], K. Weigel[1], H. Bovensmann[1], S. Dhomse[1,*], K.-U. Eichmann[1], R. Kivi[2], V. Rozanov[1], H. Vömel[3], M. Weber[1], and J. P. Burrows[1]

[1]Institute of Environmental Physics (IUP), University of Bremen, Bremen, Germany
[2]Finnish Meteorological Institute, Helsinki, Finland
[3]Meteorological Observatory Lindenberg, Deutscher Wetterdienst, Lindenberg, Germany
[*]now at: School of Earth and Environment, University of Leeds, Leeds, UK

Received: 25 August 2010 – Accepted: 3 September 2010 – Published: 8 September 2010

Correspondence to: A. Rozanov (alexei.rozanov@iup.physik.uni-bremen.de)

Published by Copernicus Publications on behalf of the European Geosciences Union.

Abstract

This study describes the retrieval of water vapor vertical distributions in the upper troposphere and lower stratosphere (UTLS) altitude range from space-borne observations of the scattered solar light made in limb viewing geometry and presents first results using measurements from SCIAMACHY. In the previous publications, the retrieval of water vapor vertical distributions has been achieved exploiting either the emitted radiance leaving the atmosphere or the transmitted solar radiation. In this study the scattered solar radiation is used as a new source of information on the water vapor content in the UTLS region. A recently developed retrieval algorithm utilizes the differential absorption structure of the water vapor in 1353–1410 nm spectral range and yields the water vapor content in 11–25 km altitude range. In this study the retrieval algorithm is successfully applied to SCIAMACHY limb measurements and the resulting water vapor profiles are compared to in situ balloon-borne observations. The results from both satellite and balloon-borne instruments are found to agree typically within 20%.

1 Introduction

A need for a good knowledge of stratospheric and upper tropospheric water vapor contents is well justified due to its major role in determining the radiative and chemical properties of the Earth's atmosphere. Water vapor plays an important role in the Earth's radiative budget affecting the climate (de F. Forster and Shine, 1999; Solomon et al., 2010). In the troposphere water vapor is one of the major and natural greenhouse gases and an important part of the hydrological cycle. It contributes to stratospheric cooling and is responsible for ozone destruction by providing odd hydrogen and participating in the formation of PSCs, see e.g. Stenke and Grewe (2005). Especially in the upper troposphere and lower stratosphere (UTLS) region water vapor can be used as a tracer to study atmospheric dynamics and stratosphere-troposphere exchange processes (Pan et al., 2007). In the tropical lowermost stratosphere observed water vapor changes are indicators for changes in the tropical upwelling, relevant for stratospheric entry of many trace species, and long-term changes in the stratospheric circulation (Randel et al., 2006; Dhomse et al., 2008).

Information on water vapor is commonly obtained by passive remote sensing in the infrared or microwave spectral ranges or from in situ measurements. Passive remote sensing technique find the widest application in space-borne observations. A variety of satellite instruments used to detect water vapor and their measurement principles are briefly discussed below. Besides the space-borne observations, passive remote sensing is also reported to be used for water vapor measurements by balloon, aircraft, and ground-based instruments (Friedl-Vallon et al., 2004; Vasic et al., 2005; Deuber et al., 2004; Nedoluha et al., 1995). In situ observations are usually performed from balloon or aircraft using FISH (Zöger et al., 1999) or FLASH (Sitnikov et al., 2007) sensors or frost point hygrometers (Vömel et al., 2007b). Furthermore, water vapor can be measured by active remote sensing with lidars (Argall et al., 2007; Kiemle et al., 2008).

Balloon and ground-based soundings are commonly used to determine 1-D distributions of water vapor on a continuous time basis and thus are very interesting for local trend analyses. From aircraft a two dimensional section of the water vapor distribution in the atmosphere along the flight track is obtained. Space-borne observations provide the only source of a long-term global information.

In the last decades several satellite instruments capable to measure vertical distributions of the water vapor have been put in operation. Most of these instruments either measure the direct solar light transmitted through the Earth's atmosphere in solar occultation mode or collect the radiance emitted by the atmospheric species in limb or nadir viewing geometry. Measurements of water vapor distributions in solar occultation geometry are currently being performed by ACE-FTS (Boone et al., 2005) and ACE-MAESTRO (Sioris et al., 2010) instruments onboard SCISAT and SCIAMACHY onboard ENVISAT. Previously this kind of measurements was done by HALOE (Harries et al., 1996), SAGE II (Thomason et al., 2004), SAGE III (Thomason et al., 2010), POAM III (Boone et al., 2005), and ILAS II (Nakajima et al., 2006) instruments. Measurements of the radiance emitted by the Earth's atmosphere, are performed by Microwave Limb Sounder onboard the Aura satellite (Read et al., 2007), SMR onboard Odin (Urban et al., 2007), and MIPAS onboard ENVISAT (Milz et al., 2005) in the limb viewing geometry. Previously this kind of measurements was done by Microwave Limb Sounder onboard UARS (Harwood et al., 1993) and JEM/SMILES on the International Space Station (Kikuchi et al., 2010). Nadir-viewing instruments observing the emitted radiation in the infrared spectral range are AIRS onboard the Aqua satellite (Hagan et al., 2004) and IASI onboard MetOp (Pougatchev et al., 2009). SCIAMACHY (Burrows et al., 1995) is the first space-borne instrument providing the possibility to retrieve vertical distributions of the water vapor from observations of the scattered solar light performed in limb viewing geometry. As discussed below SCIAMACHY retrievals have maximum sensitivity in UTLS altitude range and provide, thus, a new and complementary source of information on UTLS water vapor which has never been used before.

In this study we provide a short description of the key aspects of the SCIAMACHY limb observations and describe in detail the new retrieval approach. In addition, we provide an analysis of the sensitivity of retrievals and the relative influence of key atmospheric parameters upon the retrieved water vapor profiles. Finally, we present a first verification of the retrieved vertical profiles by comparing with measurements made by balloon-borne in situ sensors.

2 SCIAMACHY limb observations

The Scanning Imaging Absorption spectroMeter for Atmospheric CHartographY (SCIAMACHY) (Burrows et al., 1995; Bovensmann et al., 1999), is a national contribution to the payload on the European Environmental Satellite (ENVISAT) launched on 1 March 2002. It is part of a new-generation of space-borne instruments making spectrally resolved measurements in several different viewing modes: alternate nadir and limb observations of the solar radiation scattered in the atmosphere or reflected by the

AMTD
3, 4009–4057, 2010

Earth's surface as well as observations of the light transmitted through the atmosphere during the solar and when feasible lunar occultations. The SCIAMACHY instrument is a passive imaging spectrometer comprising 8 spectral channels covering a wide spectral range from 214 to 2380 nm. Each spectral channel comprises a grating spectrometer equipped with a 1024 element diode array as a detector. For the current study only measurements in the spectral channel 6 (1050–1700 nm) are used. The spectral resolution is about 1.5 nm and the spectral sampling is about 0.75 nm.

In the limb viewing geometry the SCIAMACHY instrument observes the atmosphere tangentially to the Earth's surface starting at about 3 km below the horizon, i.e., when the Earth's surface is still within the field of view of the instrument, and then scanning vertically up to the top of the atmosphere (about 100 km tangent height). At each tangent height a horizontal scan lasting 1.5 s is performed followed by an elevation step of about 3.3 km. No measurements are performed during the vertical repositioning. Thus, a limb observation sequence is performed with a vertical sampling of 3.3 km. In the altitude range relevant for this study, most typical tangent heights of limb measurements are located around 12.0, 15.3, 18.9, 21.9, and 25.2 km. The vertical instantaneous field of view of the SCIAMACHY instrument is about 2.6 km at the tangent point. Although the horizontal instantaneous field of view of the instrument is about 110 km at the tangent point, the horizontal cross-track resolution is mainly determined by the integration time during the horizontal scan reaching typically about 240 km. For a typical limb measurement, the observed signal integrated by the instrument is readout four times per horizontal scan that results in four independent limb radiance profiles obtained during a vertical scan. These four radiance profiles are often referred to as the azimuthal measurements. The entire distance at the tangent point covered by the horizontal scan is about 960 km. The horizontal along-track resolution is estimated to be about 400 km.

The signal to noise ratio of SCIAMACHY limb spectra decreases with increasing tangent height ranging from 400 to 700 near 1400 nm in the UTLS altitude region. Details about signal to noise characteristics of the SCIAMACHY instrument can be found in Noël et al. (1998).

AMTD
3, 4009–4057, 2010

Throughout this study, SCIAMACHY Level 1 data of version 6.03 are used with all calibration steps applied in the extractor software.

3 Retrieval approach

3.1 Selection of the spectral range

Because of the multiple scattering in the Earth's atmosphere, the scattered solar light detected by a satellite instrument in the limb viewing geometry contains information on the amount of atmospheric species not only in altitude layers intersected by the instrument line of sight but also in layers far below the tangent point. As a result of an increasing optical depth of the observed air mass and frequency of clouds in the lower atmosphere, the light collected by the instrument at lower tangent heights (below about ~ 10 km) typically originates from upper altitudes rather than from the tangent point area. Thus, atmospheric species in the lower atmosphere can not be retrieved in a usual way. Influence of lower atmospheric abundances upon measurements at upper tangent heights is almost negligible when observing atmospheric species with maximum number densities in the stratosphere and relatively small amounts in the lower atmosphere, such as, for example, O_3, NO_2, and BrO. However, this issue becomes problematic for species as water vapor exhibiting low abundances in the stratosphere and very high number densities in the lower atmosphere. For these species, the signal from the lower troposphere can dominate even in stratospheric observations.

In this study the contribution of the lower tropospheric water vapor in the limb signal observed at upper tangent heights is suppressed by selecting a spectral range within a strong water vapor absorption band. As a result of the strong absorption the effective path lengths of photons in the lower troposphere become shorter and the number of photons being multiply scattered within the troposphere and then entering the instrument field of view is decreased compared to weaker bands. This is illustrated in Fig. 1. The upper panel shows simulated sun normalized limb radiance in spectral channel 6 of SCIAMACHY at a tangent height of 12 km. The simulation is done with the SCIATRAN radiative transfer model (Rozanov et al., 2005; Rozanov, 2010) assuming a vertical distribution of the water vapor according to the US Standard 1976 model atmosphere (Committee on Extension to the Standard Atmosphere, 1976). In the lower panel of Fig. 1 the effect of stratospheric and tropospheric water vapor abundances upon the simulated limb radiance is illustrated. Absolute differences in the sun normalized radiance due to doubling of stratospheric (above 10 km) and tropospheric (below 10 km) water vapor amounts are depicted by blue and red curves, respectively. Positive differences mean a decrease in the simulated radiance with respect to the unperturbed simulation shown in the upper panel of the figure. The spectral interval for the retrieval is selected to ensure maximum response of the observed radiance to water vapor variations in the upper layers (i.e., above 10 km) and minimum response to variations of the lower tropospheric water vapor (i.e., below 10 km). The optimal spectral range marked in Fig. 1 by grey shadings is found to be between 1353 and 1410 nm.

3.2 Inversion technique

In this study vertical distributions of water vapor are retrieved employing the so-called global fit approach. The basic idea of this method is, first, to establish a linear relationship between measured radiances and atmospheric parameters to be retrieved, and then solve the obtained linear inverse problem employing a regularized least-square fit. A widely known implementation of the regularized least-square fit commonly referred to as the optimal estimation method with the maximum a posteriori information is discussed in detail by Rodgers (2000).

For atmospheric remote sensing observations a (non-linear) relation between measured radiances and atmospheric parameters is provided by the radiative transfer equation which in the most general representation can be written as follows:

$$\boldsymbol{y} = \boldsymbol{F}\left(\boldsymbol{x};\, \hat{\boldsymbol{x}}\right) \tag{1}$$

where the mapping $\boldsymbol{F}$ represents the radiative transfer operator, also referenced as the forward model operator, $\boldsymbol{y}$ is the measurement vector, $\boldsymbol{x}$ is the state vector containing the atmospheric parameters to be retrieved, and $\hat{\boldsymbol{x}}$ contains the parameters which affect the simulated radiance but can not be obtained from the measurements. A linearized radiative transfer equation is obtained employing the Taylor series expansion around an initial guess atmospheric state, $\boldsymbol{x}_a$, (also referred to as the a priori state vector) which is the best beforehand estimator of the true solution. Neglecting the higher order terms in the Taylor series expansion the following linear relation between measured radiances and atmospheric parameters to be retrieved is obtained:

$$\boldsymbol{y} = \boldsymbol{F}(\boldsymbol{x}_a) + \left.\frac{\partial \boldsymbol{F}(\boldsymbol{x})}{\partial \boldsymbol{x}}\right|_{\boldsymbol{x}=\boldsymbol{x}_a} \times (\boldsymbol{x} - \boldsymbol{x}_a) + \epsilon \tag{2}$$

where ϵ contains the linearization error, measurement errors, and error due to unknown atmospheric parameters which can not be retrieved. For simplicity reasons we assume here and everywhere below $\hat{\boldsymbol{x}} = \hat{\boldsymbol{x}}_a$ and skip the explicit notation of the dependence on $\hat{\boldsymbol{x}}_a$.

Neglecting all errors the linearized inverse problem is written as

$$\boldsymbol{y} = \boldsymbol{F}(\boldsymbol{x}_a) + \mathbf{K}(\boldsymbol{x} - \boldsymbol{x}_a). \tag{3}$$

where

$$\mathbf{K} \equiv \left.\frac{\partial \boldsymbol{F}(\boldsymbol{x})}{\partial \boldsymbol{x}}\right|_{\boldsymbol{x}=\boldsymbol{x}_a} \tag{4}$$

is the Jacobian matrix also referred to as the weighting function matrix. The linear inverse ill-posed problem represented by Eq. (3) is solved in the least squares sense employing the generalized Tikhonov regularization:

$$\left\|\boldsymbol{F}(\boldsymbol{x}_a) + \mathbf{K}(\boldsymbol{x} - \boldsymbol{x}_a) - \boldsymbol{y}\right\|^2_{\mathbf{P}} + \left\|(\boldsymbol{x} - \boldsymbol{x}_a)\right\|^2_{\mathbf{Q}} \longrightarrow \min. \tag{5}$$

AMTD
3, 4009–4057, 2010

Here, $\mathbf{Q}$ is a constraint matrix for the state vector and $\mathbf{P}$ (following notations from Rodgers, 2000; $\mathbf{P}=\mathbf{S}_{\varepsilon}^{-1}$) is the inverse error covariance matrix of the measurement vector $\boldsymbol{y}$. The matrix $\mathbf{S}_{\varepsilon}$ is also often referred to as the noise covariance matrix. In the framework of the widely known optimal estimation method with the maximum a posteriori information, as described by Rodgers (2000), the state vector constraint matrix, $\mathbf{Q}$, is represented by the inverse a priori covariance matrix, i.e., using the notations from Rodgers (2000) $\mathbf{Q}=\mathbf{S}_{a}^{-1}$.

The solution of the linear inverse problem given by Eq. (5) is obtained as follows:

$$\boldsymbol{x} = \boldsymbol{x}_{\mathrm{a}} + \left(\mathbf{K}^{T}\ \mathbf{P}\ \mathbf{K} + \mathbf{Q}\right)^{-1} \mathbf{K}^{T}\ \mathbf{P}\left(\boldsymbol{y} - F(\boldsymbol{x}_{\mathrm{a}})\right) \tag{6}$$

To account for the non-linearity of the inverse problem, the Gauss–Newton iterative approach is employed. At $(i+1)$-th iterative step this approach results in the following solution:

$$\boldsymbol{x}_{\mathrm{i+1}} = \boldsymbol{x}_{\mathrm{a}} + \left(\mathbf{K}_{\mathrm{i}}^{T}\ \mathbf{P}\ \mathbf{K}_{\mathrm{i}} + \mathbf{Q}\right)^{-1} \times \mathbf{K}_{\mathrm{i}}^{T}\mathbf{P}(\boldsymbol{y} - F(x_{\mathrm{i}}) + \mathbf{K}_{\mathrm{i}}(\boldsymbol{x}_{\mathrm{i}} - \boldsymbol{x}_{\mathrm{a}})) \tag{7}$$

The iterative process is stopped if the maximum difference between the components of the solution vector at two subsequent iterative steps does not exceed 1%. Typically 5–7 iterations are required to achieve convergence.

3.2.1 Retrieval implementation and parameter settings

The retrieval algorithm used in this study to gain vertical distributions of water vapor from SCIAMACHY limb measurements exploits the spectral information between 1353 and 1410 nm. Summarizing the discussion in Sect. 3.1 usage of this spectral interval maximizes sensitivity to the stratospheric water vapor and reduces the influence of the lower troposphere. As pointed out in Sect. 2, a typical SCIAMACHY limb observation comprises a series of spectral measurements performed at tangent heights between about −3 and 100 km. However, spectra at upper tangent heights are too noisy whereas measurements at lower tangent heights are contaminated by clouds and saturations effects. Therefore only the measurements at tangent heights between about 10 and 25 km are considered in the retrieval process. In addition to those from water vapor, absorption bands of methane are included in the fit procedure. Although the methane absorption is much weaker than that of the water vapor, this improves the spectral fits especially at lower tangent heights. A reliable retrieval of methane is, however, not possible.

As implemented in many other retrieval algorithms, the inverse problem in this study is formulated for logarithms of measured radiances rather than radiances themselves. As shown in previous studies (Klenk et al., 1982; Hoogen et al., 1999; Rozanov and Kokhanovsky, 2008), this approach increases the linearity of the inverse problem resulting in smaller linearization errors. The solar Fraunhofer structure is accounted for by dividing limb spectra at each tangent height by the solar spectrum. The latter is measured by SCIAMACHY once a day. To reduce the influence of instrument calibration effects as well as broadband spectral features due to unknown atmospheric parameters such as surface albedo and aerosols only the differential absorption structure is considered in the retrieval. This is done by subtracting a cubic polynomial from all spectra used in the retrieval.

Following the discussion above, the measurement vector $\boldsymbol{y}$ is created by first logarithmizing limb radiances and solar spectrum, then subtracting from the resulting spectra a cubic polynomial:

$$\hat{I}_\mathrm{n}(\lambda) = \ln I_\mathrm{n}(\lambda) - \sum_{i=0}^{3} a_{\mathrm{n},i}\,\lambda^i \quad n = 1,\ \ldots,\ N, \tag{8}$$

$$\hat{I}_\mathrm{sol}(\lambda) = \ln I_\mathrm{sol}(\lambda) - \sum_{i=0}^{3} a_{\mathrm{sol},i}\lambda^i,$$

where N is the number of tangent heights in the selected altitude region ($\sim$ 12–25 km), and ratioing finally the limb radiances to the solar spectrum:

$$y_\mathrm{n}(\lambda) = \hat{I}_\mathrm{n}(\lambda) - \hat{I}_\mathrm{sol}(\lambda). \tag{9}$$

AMTD
3, 4009–4057, 2010

UTLS water vapor from SCIAMACHY limb measurements

A. Rozanov et al.

The spectral signals $y_n(\lambda)$ obtained in this way are often referred to as the differential logarithmic spectra or differential optical depths. Thus, the measurement vector $\boldsymbol{y}$ in Eq. (7) contains differential logarithmic signals at all spectral points between 1353 and 1410 nm obtained at all tangent heights between 12 and 25 km:

$$\boldsymbol{y} = [y_1(\lambda_1), \ldots, y_1(\lambda_L), \ldots, y_N(\lambda_1), \ldots, y_N(\lambda_L)]^T, \tag{10}$$

where L is the number of spectral points in the considered spectral range (1353–1410 nm).

Similarly to the measurement vector $\boldsymbol{y}$, the model vector $\boldsymbol{F}(x_i)$, which is the result of the radiative transfer operator applied to a known atmospheric state, contains differential logarithmic spectra of the simulated sun normalized radiance at all considered tangent heights:

$$\boldsymbol{F}(x_i) = \left[\hat{I}_1^{\mathrm{sim}}(\lambda_1), \ldots, \hat{I}_1^{\mathrm{sim}}(\lambda_L), \ldots, \hat{I}_N^{\mathrm{sim}}(\lambda_1), \ldots, \hat{I}_N^{\mathrm{sim}}(\lambda_L)\right]^T, \tag{11}$$

where $\hat{I}_n^{\mathrm{sim}}(\lambda)$ is obtained from the simulated sun normalized radiance, $I_n^{\mathrm{sim}}(\lambda)$, in exactly the same way as described by Eq. (8) for the measured limb radiance.

To ensure that the resulting vertical profiles are always non-negative the inverse problem given by Eq. (3) is solved for logarithms of trace gas number densities instead of the number densities themselves, i.e., the state vector $\boldsymbol{x}$ contains logarithms of water vapor and methane number densities at all altitude layers considered in the forward model.

Although the spectral interval used in this study is selected to reduce the influence of the lower tropospheric water vapor, under certain conditions its contribution to the measured signal can still remain non-negligible (see Sect. 4.1 for details). To account for this contribution two additional components are appended to the state vector, namely, the tropospheric water vapor column, t, and the surface albedo, A.

Summing up the discussion above, the state vector is written as

$$\boldsymbol{x} = [\ln p_w(z_1), \ldots, \ln p_w(z_J), \ln p_m(z_1), \ldots, \ln p_m(z_J), t, A]^T, \tag{12}$$

where $p_w(z)$ and $p_m(z)$ are the number densities of the water vapor and methane, respectively, z is the altitude grid of the forward model, and J is the total number of the altitude levels. In the altitude range relevant for the water vapor retrieval an equidistant hight grid with 1 km spacing is used. The tropospheric column, t, is defined as the integral of the water vapor number density profile between the surface and 9 km altitude. In a discrete representation it is written as

$$t = \sum_{j=1}^{J_t} p_w\left(z_j\right) \Delta z_j . \quad (13)$$

Here, $z_1 = 0$ km, $z_{J_t} = 9$ km, and Δz_j are the geometrical thicknesses of the corresponding altitude layers.

The weighting function matrix **K** describes variations of the radiance logarithms at considered tangent heights and spectral points due to variations of the retrieved parameters (water vapor and methane number densities at different altitude levels, tropospheric column of water vapor, and surface albedo). Similarly to the measurement vector $\boldsymbol{y}$ and model vector $\boldsymbol{F}(x_i)$, the weighting functions need to be transformed into the differential logarithmic representation. Taking into account Eq. (4) this is done as follows:

$$K_{n,j}(\lambda) = \frac{1}{I_n^{sim}(\lambda)} \frac{\partial I_n^{sim}(\lambda)}{\partial x_j} - \sum_{i=0}^{3} a_{n,i}\, \lambda^i , \qquad n = 1, \ldots, N, \quad j = 1, \ldots, 2J+2, \quad (14)$$

where x_j are the components of the state vector $\boldsymbol{x}$ as defined by Eq. (12). The row index of the matrix elements is running with the spectral point number and with the tangent height similar to the measurement vector, see Eq. (10). The column index is running with the retrieval parameter number (altitude layers for the water vapor and methane, water vapor tropospheric column, and surface albedo) similar to the state vector, see Eq. (12).

Synthetic limb radiance spectra as well as appropriate weighting functions are calculated with the SCIATRAN radiative transfer model (Rozanov et al., 2005; Rozanov,

2010) taking into account refractive ray tracing. The limb radiance is simulated in the approximate spherical mode employing the combined differential-integral approach. In the framework of this method the single scattering contribution is treated fully spherically. For the multiply scattered light a pseudo-spherical model is used first to obtain the multiple scattering source function at each point along the instrument line of sight. Doing this the solar zenith angle and viewing direction are set in accordance with a spherical ray tracing. Finally, the multiple scattering contributions are integrated along the line of sight taking into account the sphericity of the atmosphere. A detailed description of this approach can be found in Rozanov et al. (2001). Weighting functions for trace gas number densities are calculated solving the linearized radiative transfer equation (Rozanov and Rozanov, 2007) in the single scattering approximation. It is worth noticing here that the single scattering approximation means that contributions of all atmospheric layers below the instrument field of view (i.e., contributions of the lower tropospheric water vapor) are neglected and the corresponding elements of the weighting function matrix are zero. Obviously, this method is unsuitable to account for tropospheric or surface parameters. Therefore, the numerical perturbation method is used to obtain weighting functions for the tropospheric water vapor column and for the surface albedo.

Before the main retrieval is performed all spectra are corrected for a possible wavelengths misalignment that can be caused by a changing illumination of the instrument entrance slit during the vertical scan. This is done for each tangent height independently minimizing the following quadratic form with respect to parameters s_i, c_{sim}, and c_{sol}:

$$\left\| \hat{I}_{\mathrm{n}}(\lambda) - \hat{I}_{\mathrm{sol}}(\lambda) - \hat{I}_n^{\mathrm{sim}}(\lambda) - \sum_{i=1}^{4} s_i \, W_{\mathrm{n},i}(\lambda) - c_{\mathrm{sim}} \frac{\partial I_{\mathrm{n}}^{\mathrm{sim}}(\lambda)}{\partial \lambda} - c_{\mathrm{sol}} \frac{\partial \hat{I}_{\mathrm{sol}}(\lambda)}{\partial \lambda} \right\|^2 \longrightarrow \min. \quad (15)$$

AMTD
3, 4009–4057, 2010
UTLS water vapor from SCIAMACHY limb measurements
A. Rozanov et al.

Here, the weighting functions for the water vapor and methane number densities are vertically integrated, e.g., for the water vapor

$$W_{n,1}(\lambda) = \sum_{j=1}^{J} K_{n,j}(\lambda)\Delta z_j, \tag{16}$$

where $K_{n,j}(\lambda)$ is defined according to Eq. (14), whereas the weighting functions for the tropospheric water vapor column and for the surface albedo are kept unchanged, e.g.,

$$W_{n,3}(\lambda) = K_{n,2J+1}(\lambda). \tag{17}$$

The coefficients c_{sim} and c_{sol} represent shift corrections for the simulated and the solar spectrum with respect to the measured spectrum, respectively. Although the fit parameters are tangent height dependent, subscript n is omitted here for simplicity.

The shift coefficients obtained from this spectral fit are used to correct spectral misalignments of the simulated and solar spectra as follows:

$$\hat{I}_n^{\mathrm{sim}}(\lambda) = \hat{I}_n^{\mathrm{sim}}(\lambda) + c_{\mathrm{sim}} \frac{\partial \hat{I}_n^{\mathrm{sim}}(\lambda)}{\partial \lambda} \tag{18}$$

and

$$\hat{I}_{\mathrm{sol}}(\lambda) = \hat{I}_{\mathrm{sol}}(\lambda) + c_{\mathrm{sol}} \frac{\partial \hat{I}_{\mathrm{sol}}(\lambda)}{\partial \lambda}. \tag{19}$$

These corrected spectra are used then to create the measurement and model vectors as defined by Eqs. (9) and (11), respectively. The scaling factors s_i are auxiliary parameters that are not used further.

In the course of the main retrieval procedure the non-linear inverse problem defined by Eq. (1) is solved according to Eq. (7) with weighting function matrix defined by Eq. (14) and measurement, model, and state vectors defined by Eqs. (10), (11), and (12), respectively. The noise covariance and solution constraint matrices (**P** and **Q**, respectively) are set up as described below.

AMTD

3, 4009–4057, 2010

UTLS water vapor from SCIAMACHY limb measurements

A. Rozanov et al.

The diagonal elements of the noise covariance matrix, **P**, are set according to root mean squares of the fit residuals obtained minimizing the quadratic form given by Eq. (15) at each tangent height. The off-diagonal elements of this matrix are set to zero assuming the measurement noise to be spectrally uncorrelated. The solution constraint matrix, **Q**, consist of two matrices, namely, the inverse a priori covariance matrix as commonly used in the optimal estimation approach (Rodgers, 2000) and a smoothness constraint matrix:

$$\mathbf{Q} = \mathbf{S}_\mathrm{a}^{-1} + \mathbf{R}^T\mathbf{R}. \tag{20}$$

The usage of smoothness constraints is advantageous to suppress oscillations of the solution without overconstraining it when retrieving at a fine altitude grid. For each atmospheric species included in the retrieval (water vapor and methane) the elements of the a priori covariance matrix are set in accordance with the following rule:

$$\{S_\mathrm{a}\}_{i,j} = \sigma_i \sigma_j \exp\left(-\frac{|z_i - z_j|}{l_\mathrm{c}}\right), \tag{21}$$

where σ_i and σ_j are a priori uncertainties at altitudes z_i and z_j, respectively, and l_c is the correlation length (set to 1.5 km in this study). The full a priori covariance matrix is formed then from the covariance matrices of both species as well as covariances of the tropospheric water vapor column, σ_t^2, and of the surface albedo, σ_A^2:

$$\mathbf{S}_\mathrm{a} = \begin{bmatrix} \mathbf{S}_\mathrm{a}^{\mathrm{H_2O}} & \mathbf{0} & \mathbf{0} & \mathbf{0} \\ \mathbf{0} & \mathbf{S}_\mathrm{a}^{\mathrm{CH_4}} & \mathbf{0} & \mathbf{0} \\ \mathbf{0} & \mathbf{0} & \sigma_t^2 & 0 \\ \mathbf{0} & \mathbf{0} & 0 & \sigma_A^2 \end{bmatrix}, \tag{22}$$

where **0** represents a zero submatrix. Cross-correlations between different species, tropospheric water vapor column, and surface albedo are not considered. A priori uncertainties are set to 300% for water vapor, 30% for methane, 100% for the tropospheric water vapor column, and 0.1 for the surface albedo. Similarly to the a priori

AMTD
3, 4009–4057, 2010

covariance matrix, matrix **R** is also block diagonal. It contains, however, zeros in place of the altitude independent parameters (tropospheric water vapor column and surface albedo):

$$\mathbf{R} = \begin{bmatrix} \mathbf{R}^{\mathrm{H_2O}} & \mathbf{0} & \mathbf{0} \\ \mathbf{0} & \mathbf{R}^{\mathrm{CH_4}} & \mathbf{0} \\ \mathbf{0} & \mathbf{0} & \mathbf{0} \end{bmatrix}. \tag{23}$$

Non-zero elements of the submatrices for each particular species are given by

$$\{\mathbf{R}\}_{j,j-1} = \frac{c_j}{z_{j-1} - z_j} \text{ and } \{\mathbf{R}\}_{j,j} = \frac{-c_j}{z_{j-1} - z_j}, \tag{24}$$

where c_j represents the smoothness coefficient and j runs through all altitude levels starting from the second one. For water vapor the smoothness coefficient increases linearly from 5 at 10 km to 10 at 30 km, while smoothness coefficient of 1 is used at all altitude layers for methane.

The spectral absorption features of the water vapor and methane are accounted for employing the correlated-k distribution scheme (Buchwitz et al., 2000) with ESFT coefficients calculated using the HITRAN 2008 database (Rothman et al., 2009). The forward model is initialized using the global pressure, temperature, and surface elevation information provided by the European Centre for Medium-Range Weather Forecasts (ECMWF) as well as trace gas vertical distributions according to the US Standard 1976 model atmosphere (Committee on Extension to the Standard Atmosphere, 1976). Furthermore, a background aerosol loading according to the LOWTRAN parameterization (Kneizys et al., 1986) is assumed. The initial value for the surface albedo is set according to the vegetation and land-use data base described by Matthews (1983). In the current study only measurements with no clouds detected above 10 km are considered. The effect of lower clouds is neglected.

Figure 2 shows example spectral fits for a SCIAMACHY limb observation performed on 27 January 2004, at 17:18:22 UTC (orbit 9986) over Boulder, CO, USA (40° N,

AMTD
3, 4009–4057, 2010

Title Page
Abstract | Introduction
Conclusions | References
Tables | Figures
◀◀ | ▶▶
◀ | ▶
Back | Close
Full Screen / Esc
Printer-friendly Version
Interactive Discussion

105° W). The spectral fits are shown for tangent heights of 12 and 21.9 km in the left and right plots, respectively. The upper panels of each plot show the measured differential logarithmic spectra as defined by Eq. (9) by red curves and the corresponding simulated spectra by green curves whereas the lower panels show fit residuals.

4 Sensitivity studies

4.1 Origin of the observed signal

This section is intended to answer the question where the scattered light detected by the SCIAMACHY instrument during a limb observation originates from. Main topics to be investigated here are the role of stratospheric aerosols, contribution due to the multiple scattering, as well as the influence of the lower atmospheric composition (below the instrument field of view) and surface properties. At first, the most typical limb observations are discussed. These are considered to be performed over regions with not too dry troposphere, surface height at about see level, and no highly reflecting thick clouds below the instrument field of view. Special cases where some of this requirements are not fulfilled are considered in the second part of this section as well as in Sect. 4.3 below.

Figure 3 shows synthetic sun normalized limb radiance simulated assuming different atmospheric compositions. The simulations are performed for a tangent height of 15 km and a solar zenith angle at tangent point of 69°. Results of the standard run considering multiple scattering, background aerosols, and a surface albedo of 0.5 are shown by the magenta line. The same simulation in single scattering approximation is shown by the blue line. Both curves lie close together indicating that the bulk of the observed limb signal is due to single scattering. Coming back to the multiply scattered radiation and turning off the stratospheric aerosols (above 10 km) the results depicted by the cyan line are obtained. A strong decrease in the intensity reveals that aerosol scattering dominates in the considered spectral range. Finally, the red line shows the

AMTD
3, 4009–4057, 2010

sun normalized intensity simulated for an aerosol-free atmosphere and non-reflecting surface (surface albedo is set to zero). This scenario represents a simulation with a strongly reduced contribution of light scattered in the lower atmosphere and/or reflected from the surface. As expected, for a typical SCIAMACHY observation the influence of the lower atmospheric composition and surface properties upon the simulated radiance is rather small.

Being crucial for absolute values of the sun normalized radiance, the exact knowledge of aerosol scattering characteristics plays, however, a rather minor role when simulating differential absorption. This is illustrated in Fig. 4 where the same simulated sun normalized radiances as in Fig. 3 are shown in the differential logarithmic representation as defined by Eq. (8). One sees that the spectral signals do not differ much any more. Absolute differences in the differential logarithmic intensities with respect to the standard scenario (shown with the magenta line in Figs. 3 and 4) are presented in Fig. 5. Here, the same color coding as above is used. The plot reveals that all considered parameters cause differences of similar magnitude which amounts to about 5–10% of the observed signal (as shown in Fig. 4).

For a typical SCIAMACHY limb observation most of the solar light penetrating into the lower troposphere is absorbed. Much more light can be scattered back into the instrument field of view if the water vapor absorption in the lower troposphere is abnormally weak. This can be the case, for example, for an extremely dry troposphere or highly reflecting surfaces with high elevations above the sea level (mountains, clouds). Under these circumstances the portion of light in the observed limb signal that has traveled long paths through the lower troposphere increases. Consequently, a stronger influence of the lower tropospheric composition and surface properties upon the retrieval is expected. This fact is illustrated in Fig. 6 that shows the weighting function for the stratospheric water vapor column (red curves) in comparison with the weighting functions for the tropospheric water vapor column (blue curves) and for the surface albedo (cyan curves). Here, the former weighting function is defined by Eq. (16) while the latter two are according to Eq. (17). Similar to previous plots, the weighting functions are

AMTD
3, 4009–4057, 2010

calculated for a tangent height of 15 km and a solar zenith angle of 69°. The left panel represents a typical SCIAMACHY limb observation, the right panel depicts a case of an abnormally weak absorption in the lower troposphere due to a reflecting surface elevated by 2 km a.s.l. (above the sea level). As discussed above, weighting functions describe variations of the observed signal due to variations in atmospheric or surface properties. Thus, a larger weighting function denotes higher influence of the corresponding parameter upon the observed signal and, consequently, upon the retrieved profiles. For a typical SCIAMACHY limb observation Fig. 6 reveals a minor role of both tropospheric water vapor column and surface albedo as their weighting functions are negligibly small in comparison with the weighting function of the stratospheric water vapor column. In contrast, for a highly elevated reflecting surface magnitudes of all weighting functions become comparable indicating a stronger influence of the lower tropospheric composition and surface properties. To account for this influence the weighting functions of the tropospheric water vapor column and of the surface albedo are included in the retrieval procedure as discussed above in Sect. 3.2.1. More quantitatively the impact of the lower tropospheric composition and surface properties upon the retrieved water vapor profiles as well as remaining retrieval errors are discussed in Sect. 4.3.

4.2 General characterization of the retrieval

A commonly used approach to characterize retrieval algorithms that employ an optimal estimation type inversion is to analyze the averaging kernels. The latter are specific to the measurement setup, algorithm implementation, and retrieval parameter settings. For observations of the scattered solar light performed by space-borne instruments in limb viewing geometry, averaging kernels in the relevant altitude region are distinctly peaked at altitudes where a bulk of information is originating from. The shape of averaging kernels provides an information on the vertical sensitivity and resolution of the measurement-retrieval system as well as on the contribution of a priori information to retrieved profiles.

AMTD
3, 4009–4057, 2010

Figure 7 shows parameters essential for the retrieval characterization for a limb observation performed in winter over Boulder, CO, USA (39.95° N, 105.2° W) at a solar zenith angle of about 65°. Panel (a) shows the water vapor number density profile typical for this location and season. The corresponding averaging kernels are shown in panel (b). The colored numbers in the right-hand side of the averaging kernel plot denote the altitudes for which the averaging kernels are calculated. The averaging kernels for altitudes close to measurement tangent heights show well pronounced peaks near the tangent point altitude. On the contrary, the averaging kernels for intermediate altitude levels are substantially broader with much less distinct peaks indicating a redistribution of the information between measurement tangent heights. The altitude region where the retrieval has the best sensitivity can be identified as 11 to 23 km. Here, the averaging kernels are large and peak at their nominal altitudes. At higher altitudes the averaging kernels become broader which is associated with the smoothing error increasing with the altitude. The peak altitudes remain around 22 km almost independent of the nominal altitude of the averaging kernels which indicates that the water vapor signal observed at tangent heights above 23 km originates mostly from the lower layers. Bellow 11 km, the averaging kernels still have pronounced peaks which, however, are clearly displaced upwards indicating that information from upper altitudes dominates the retrieved profile.

More quantitative characterization of the inversion quality can be done by looking at the theoretical precision of the retrieval and the measurement response function. The former is given by the square root of the diagonal elements of the solution covariance matrix (Rodgers, 1976, 1990) and describes the total retrieval error (i.e., sum of the noise and smoothing errors). The measurement response function is given by the area of the averaging kernels and describes the relative contribution of the measurements and a priori information to the retrieved profile. Values close to one indicate that most of the information comes from the measurement and the corresponding retrieval can be considered to be unbiased by a priori information. Both the theoretical precision (red curve) and measurement response function (light blue curve) are shown in panel (c) of

AMTD
3, 4009–4057, 2010

Fig. 7. The theoretical precision of the retrieval is between 10 and 20% in the entire altitude range considered by the retrieval. The measurement response is close to 1 at all altitudes below 21 km slightly decreasing above.

The vertical resolution of the retrieval is characterized by the width of the averaging kernels which, however, is rather difficult to define quantitatively. Following other authors, e.g., Haley et al., 2004; Sofieva et al., 2004; Krecl et al., 2006, we will employ the Backus and Gilbert approach (Backus and Gilbert, 1970) using the following function called spread to define the averaging kernel width:

$$s(z) = 12 \frac{\int \left(z - z'\right)^2 \mathbf{A}^2 \left(z, z'\right) \, d\, z'}{\left[\int \left|\mathbf{A}(z, z')\right| \, d\, z'\right]^2}. \tag{25}$$

Panel (d) of Fig. 7 shows a typical spread function calculated according to Eq. (25) for the averaging kernels plotted in panel (b). It follows that in the high sensitivity altitude range the vertical resolution of the retrieval is about 2 to 3 km near the measurement tangent point altitudes and ranges between 4 and 6 km for intermediate layers. Above 23 km where the sensitivity of the measurements starts to decrease a stronger smoothing occurs leading to a rapid decrease of the vertical resolution. It is also worth noticing that above 23 km the averaging kernel peaks are displaced from their nominal altitudes. The peak displacement increases the spread calculated according to Eq. (25) significantly. This is why the apparent width of the averaging kernels is no longer related to their spread and it becomes questionable if the Backus and Gilbert approach can still be used to characterize the vertical resolution of the retrieval.

Another way to investigate the retrieval performance is to simulate limb observations assuming different vertical distributions of the water vapor and then perform synthetic retrievals with the same a priori information as in real retrievals. The results of these synthetic retrievals are shown in Fig. 8. In the left panel of the plot the true water vapor profiles used for simulations are depicted by colored solid lines whereas the retrieved profiles are shown by the asterisks of the corresponding colors. The dashed black line depicts the a priori profile. The true profiles shown by the blue and red lines are obtained from a climatological model for the winter at latitudes of 35° N and 65° N, respectively, whereas the profiles shown by the magenta and light blue lines are obtained scaling the above described climatological profiles. The scaling factors of 2 and 0.5, respectively, are selected arbitrarily. The right panel of Fig. 8 shows the relative differences between the retrieved and true profiles of the water vapor. For smooth true profiles (as shown by blue and magenta lines) the retrieval errors are very small never exceeding 20% within the sensitivity range. A quite different behavior is observed for true profiles having sharp vertical gradients in the tropopause region. Due to a lack of the vertical resolution the break-points can not be captured exactly which leads to large local differences around the tropopause altitude and cause follow-up discrepancies at other altitudes. A usual way to account for different vertical resolutions of the compared profiles is to convolve highly resolved profiles with the averaging kernels corresponding to the low resolution retrieval. Convolving the true profiles shown in Fig. 8 with the corresponding averaging kernels the results shown in Fig. 9 are obtained. Now, true and retrieved profiles agree within 10% nearly everywhere demonstrating that the discrepancies seen in Fig. 8 are mostly due to the limited vertical resolution of SCIAMACHY limb observations.

4.3 Tropospheric impact and surface effects

As discussed in Sect. 4.1, the impact of the lower tropospheric composition and surface properties upon the retrieved water vapor profiles is negligible for a typical limb observation. However, it may become significant if abnormally much light that has traveled long paths through the lower atmosphere reaches the detector. In this section we consider an example retrieval for a highly elevated surface to quantify the retrieval errors due to the lower tropospheric water vapor amount and surface properties. As illustrated below, reliable results in this case can only be obtained considering these parameters in the retrieval process.

The effect of the tropospheric water amount and of the surface parameters is investigated performing synthetic retrievals as follows. First, a limb observation is simulated

AMTD
3, 4009–4057, 2010

assuming a water vapor profile according to the US Standard model atmosphere, surface albedo of 0.5, and surface elevation of 2.2 km. The latter corresponds to an observation above the NOAA Earth System Research Laboratory in Boulder, CO, USA. The simulations are performed for a solar zenith angle of 64°. This synthetic limb observation is used then to perform a series of retrievals using various assumptions about the tropospheric water vapor amount and surface properties. As shown in Fig. 10, synthetic retrievals are performed using surface albedos of 0 and 1 (red and magenta solid lines, respectively), doubling and halving the tropospheric water vapor amount at different surface albedos (green, blue, and light blue solid lines) and raising the surface to 4 and 6 km (red and green dashed lines, respectively). Results of the complete retrieval including the weighting functions for the tropospheric water vapor column and surface albedo (as described in Sect. 3.2.1) are shown in the right panel while the left panel illustrates the errors of the basic retrieval where only the stratospheric water vapor amounts are fitted and the contributions of the tropospheric water vapor and of the surface properties are neglected. The left panel of the plot reveals that changes in atmospheric or surface parameters which decrease amount of light traveled long paths through the lower atmosphere (e.g., decrease in the surface albedo, or doubling of tropospheric water vapor amount) affect the retrieval only weakly. On the contrary, the scenarios where more light from the lower troposphere reaches the detectors (e.g., increase in the surface albedo, higher surface elevation, or halved amount of the tropospheric water vapor) cause dramatic changes in the retrieved profiles. However, as shown in the right panel of Fig. 10, this effect is almost completely accounted for if the weighting functions for the tropospheric water vapor column and for the surface albedo are included in the retrieval.

5 Comparisons

In previous sections we have analyzed the retrieval precision and investigated the influence of key atmospheric parameters upon the retrieved water vapor profiles. However,

AMTD
3, 4009–4057, 2010

there is still not enough information to assess the total error budget theoretically. Instead, in this section we estimate the total uncertainty of SCIAMACHY water vapor retrievals by comparisons with independent measurements.

To estimate the quality of single retrievals, example water vapor profiles obtained from SCIAMACHY limb observations are compared to in situ measurements performed with a balloon-borne frost point hygrometer (FPH) over Boulder, CO, USA (data provided by NOAA Earth System Research Laboratory, Global Monitoring Division). The uncertainty of balloon-borne FPH measurements is estimated to be about 10%. Further details on the instrument are presented in Vömel et al. (1995). Water vapor profiles are compared for four balloon flights performed on 2 July 2003, 8 July 2003, 20 November 2003, and 27 January 2004. The collocations are selected according to the best match principle requiring the time difference between two measurements to be within 12 h.

The results of the comparison are presented in Figs. 11 (for profiles) and 12 (for relative differences). The water vapor profiles obtained from the balloon-borne instrument are shown with dashed black lines for original profiles and with solid black lines for profiles convolved with SCIAMACHY averaging kernels. The SCIAMACHY retrievals are shown by solid lines with asterisks and corresponding a priori profiles are depicted by dashed orange lines. As discussed in Sect. 2, during each limb measurement sequence the SCIAMACHY instrument performs a horizontal across-track scan. This provides typically four independent observations per limb scan which are performed at slightly different azimuthal angles. The water vapor profiles obtained from these azimuthal measurements are shown with different colors. As measurements contaminated by high clouds are filtered out, for certain limb observations less than four profiles are retrieved (e.g., upper right panel in Figs. 11 and 12).

The comparison demonstrates the stability of single SCIAMACHY retrievals and shows good overall agreement between the SCIAMACHY and balloon profiles. In the altitude range between 14 and 25 km differences are typically below 20% getting somewhat worse for lower altitudes.

AMTD
3, 4009–4057, 2010

A more extensive verification of SCIAMACHY retrievals is performed using in situ measurements with a balloon-borne cryogenic frost point hygrometer (CFH) operated at different locations. In this study the data obtained at following balloon launch sites are considered: Boulder, CO, USA (40° N, 105° W); Heredia, Costa Rica (10° N, 84° W), Beltsville, MD, USA (39° N, 77° W); Sodankylä, Finland (67° N, 27° E); Biak, Indonesia (1° S, 136° E); Kototabang, Indonesia (0.2° S, 100° E); Ha Noi, Vietnam (21° N, 106° E); Alajuela, Costa Rica (10° N, 84° W); Lindenberg, Germany (52° N, 14° E). The uncertainty of balloon-borne CFH measurements is estimated to be about 10%. Details on the instrument and measurement campaigns can be found in Vömel et al. (2007b); Fujiwara et al. (2010); Selkirk et al. (2010). A map showing locations of the balloon launch sites and tangent points of coinciding SCIAMACHY measurements is presented in Fig. 13. The SCIAMACHY measurements are selected requiring a maximum distance of 1000 km and maximum time mismatch of 5 h (with respect to the balloon launch time). For each balloon flight several coinciding SCIAMACHY measurements might exist. In all comparisons below water vapor profiles obtained from balloon-borne instrument are convolved with SCIAMACHY averaging kernels.

Figure 14 presents a comparison of water vapor profiles obtained from balloon-borne CFH and SCIAMACHY measurements. The results are averaged over all balloon launches at all sites as shown in Fig. 13. In total 206 SCIAMACHY observations and 59 balloon flights are considered. The left panel of the plot shows average balloon-borne CFH (blue) and SCIAMACHY (red) profiles with solid lines and corresponding standard deviations with dashed lines. The right panel shows the mean relative difference between both measurements (SCIAMACHY/CFH-1) and corresponding standard deviation. The plot reveals good overall agreement between the two datasets. The results agree within 20% above 14 km and differ somewhat more below.

A similar comparison but for water vapor profiles averaged within certain zonal bands is presented in Fig. 15. Here, the same notations as in Fig. 14 are used. Upper panels show the averaged profiles from both instruments and their standard deviations, whereas lower panels show mean relative differences and corresponding standard deviations. The left panels show a comparison in the tropics (30° S–30° N) where results from 75 SCIAMACHY measurements and 20 balloon launches are considered. In this region the results from both instruments agree within 20% down to 16 km. Although between 12 and 16 km the average profiles still agree within 20–30% the standard deviations both for profiles and for relative errors increase substantially. This is because in the tropics these altitudes are located in the troposphere with an inherent high variability of water vapor content. A similar behavior has been observed in the comparison of CFH and Aura MLS results presented in Vömel et al. (2007a). The middle panels of Fig. 15 present comparison results for middle latitudes of the Northern Hemisphere (30° N–60° N) considering results from 90 SCIAMACHY measurements and 25 balloon launches. Here, an agreement within 20% is observed down to 13 km with a slight increase in relative difference below. Similarly to the tropics, a small negative bias is observed in SCIAMACHY results above 18 km. In the right panels a similar comparison for high latitudes of the Northern Hemisphere (above 60° N) is presented. Here, 41 SCIAMACHY measurements and 16 balloon launches are considered. Unlike the tropics and mid-latitudes, a smaller negative bias but higher standard deviations are observed at upper altitudes. This behavior is believed to be due to a presence of several too wet profiles in the high latitudinal data set from SCIAMACHY. Down to 14 km both datasets agree within 10% and differ by 10–40% below. Unfortunately, a removal of cloudy scenes, especially multilayer thin clouds, still remains a challenging issue. An imperfect cloud filtering is believed to be the main reason for the remaining positive peaks in the mean relative difference occurring at all latitudes (at about 15 km in tropics and 12–13 km at middle and high latitudes).

AMTD
3, 4009–4057, 2010

6 Conclusions

In contrast to space-borne observations of the emitted radiance or transmitted solar light which have been widely exploited previously, measurements of scattered solar light performed by SCIAMACHY in limb viewing geometry provide a completely new source of information on vertical distribution of water vapor in the lower stratosphere and upper troposphere (UTLS) altitude region. In this study we suggest a new method capable to retrieve UTLS water vapor contents from this kind of measurements. The paper describes an optimal selection of the spectral range and analyses contributions of different processes (multiple scattering, surface albedo, aerosols) into the measured spectral signal. The applied retrieval algorithm is described in detail and sensitivity of retrievals is investigated. The highest sensitivity is found to be between 11 and 23 km. Using synthetic retrievals the performance of the algorithm and its weak sensitivity to major atmospheric and surface parameters other than UTLS water vapor content is demonstrated.

The new method is successfully applied to SCIAMACHY limb observations. A verification of the retrieval results is performed using data from in situ balloon-borne measurements with frost point or cryogenic frost point hygrometers. The comparison reveals an overall good agreement between the SCIAMACHY and balloon instruments in the relevant altitude range. The datasets are found to agree within 10–20% although a slight negative bias is often seen in SCIAMACHY results above 18 km. This bias is subject to further investigation. An extensive validation of UTLS water vapor profiles retrieved from SCIAMACHY limb measurements is ongoing.

Acknowledgements. We thank Sam Oltmans and Dale F. Hurst (NOAA Earth System Research Laboratory, Global Monitoring Division) for providing NOAA FPH profile data. The CFH measurements from Beltsville, MD were made at the Howard University Beltsville Campus during the WAVES field campaigns supported by the NASA Atmospheric Chemistry Program and led by David Whiteman of NASA/GSFC, Everette Joseph and Belay Demoz of Howard University. The CFH measurements at Biak, Kototabang, and Ha Noi were made under the Soundings of Ozone and Water in the Equatorial Region (SOWER) project led by Fumio Hasebe (Hokkaido

Discussion Paper | Discussion Paper | Discussion Paper | Discussion Paper |

AMTD

3, 4009–4057, 2010

UTLS water vapor from SCIAMACHY limb measurements

A. Rozanov et al.

University), Masato Shiotani (Kyoto University), and Masatomo Fujiwara (Hokkaido University). We are thankful to ECMWF for providing pressure, temperature, and surface elevation information (ECMWF Special Project SPDECDIO). Some data shown here were calculated on German HLRN (High-Performance Computer Center North) and NIC/JUMP (Forschungszentrum Jülich Multiprocessor System). Services and support are gratefully acknowledged. This study has been funded by DLR Space Agency (Germany), grant 50EE0727, European Commission EC SCOUT-O3, and by the University and State of Bremen. Part of this work has been supported by the DFG Research Unit FOR 1095 “Stratospheric Change and its role for Climate Prediction (SHARP)” (Project: GZ WE 3647/3-1).

References

Argall, P. S., Sica, R., Bryant, C., Algara-Siller, M., and Schijns, H.: Calibration of the Purple Crow Lidar Raman water vapour and temperature measurements, Can. J. Phys., 85, 119–129, 2007. 4011

Backus, G. E. and Gilbert, F. E.: Uniqueness in the inversion of inaccurate gross Earth data, Philos. T. Roy. Soc. Lond. A, 266, 123–192, 1970. 4029

Boone, C. D., Nassar, R., Walker, K. A., Rochon, Y., McLeod, S. D., Rinsland, C. P., and Bernath, P. F.: Retrievals for the atmospheric chemistry experiment Fourier-transform spectrometer, Appl. Optics, 44, 7218–7231, 2005. 4011, 4012

Bovensmann, H., Burrows, J. P., Buchwitz, M., Frerick, J., Noël, S., Rozanov, V. V., Chance, K. V., and Goede, A. P. H.: SCIAMACHY: Mission objectives and measurement modes, J. Atmos. Sci., 56, 127–149, 1999. 4012

Buchwitz, M., Rozanov, V. V., and Burrows, J. P.: A correlated-k distribution scheme for overlapping gases suitable for retrieval of atmospheric constituents from moderate resolution radiance measurements in the visible/near-infrared spectral region, J. Geophys. Res., 105, 15247–15261, 2000. 4024

Burrows, J. P., Hölzle, E., Goede, A. P. H., Visser, H., and Fricke, W.: SCIAMACHY – Scanning Imaging Absorption Spectrometer for Atmospheric Chartography, Acta Astronaut., 35, 445–451, 1995. 4012

Committee on Extension to the Standard Atmosphere: U.S. Standard Atmosphere, 1976, Government Printing Office, Washington, DC, 1976. 4015, 4024

AMTD

3, 4009–4057, 2010

UTLS water vapor from SCIAMACHY limb measurements

A. Rozanov et al.

de F. Forster, P. M. and Shine, K. P.: Stratospheric water vapour changes as a possible contributor to observed stratospheric cooling, Geophys. Res. Lett., 26, 3309–3312, doi:10.1029/1999GL010487, 1999. 4010

Deuber, B., Kämpfer, N., and Feist, D. G.: A new 22-GHz Radiometer for Middle Atmospheric Water Vapour Profile Measurements, IEEE T. Geosci. Remote, 42, 974–984, doi:10.1109/TGRS.2004.825581, 2004. 4011

Dhomse, S., Weber, M., and Burrows, J.: The relationship between tropospheric wave forcing and tropical lower stratospheric water vapor, Atmos. Chem. Phys., 8, 471–480, doi:10.5194/acp-8-471-2008, 2008. 4011

Friedl-Vallon, F., Maucher, G., Kleinert, A., Lengel, A., Keim, C., Oelhaf, H., Fischer, H., Seefeldner, M., and Trieschmann, O.: Design and characterisation of the ballonborne Michelson Interferometer for Passive Atmospheric Sounding (MIPAS B2), Appl. Optics, 43, 3335–3355, 2004. 4011

Fujiwara, M., Voemel, H., Hasebe, F., Shiotani, M., Ogino, S.-Y., Iwasaki, S., Nishi, N., Shibata, T., Shimizu, K., Nishimoto, E., Valverde-Canossa, J. M., Selkirk, H. B., and Oltmans, S. J.: Seasonal to decadal variations of water vapor in the tropical lower stratosphere observed with balloon-borne cryogenic frost point hygrometers, J. Geophys. Res., in press, doi:10.1029/2010JD014179, 2010. 4033

Hagan, D. E., Webster, C. R., Farmer, C. B., May, R. D., Herman, R. L., Weinstock, E. M., Christensen, L. E., Lait, L. R., and Newman, P. A.: Validating AIRS upper atmosphere water vapor retrievals using aircraft and balloon in situ measurements, Geophys. Res. Lett., 31, L21103, doi:doi:10.1029/2004GL020302, 2004. 4012

Haley, C. S., Brohede, S. M., Sioris, C. E., Griffioen, E., Murtagh, D. P., McDade, I. C., Eriksson, P., Llewellyn, E. J., Bazureau, A., and Goutail, F.: Retrieval of stratospheric O_3 and NO_2 profiles from Odin Optical Spectrograph and Infrared Imager System (OSIRIS) limb-scattered sunlight measurements, J. Geophys. Res, 109, D16303, doi:10.1029/2004JD004588, 2004. 4029

Harries, J. E., Russell III, J. M., Tuck, A. F., Gordley, L. L., Purcell, P., Stone, K., Bevilacqua, R. M., Gunson, M., Nedoluha, G., and Traub, W. A.: Validation of measurements of water vapor from the halogen occultation experiment (HALOE), J. Geophys. Res., 101, 10205–10216, 1996. 4011

Harwood, R., Carr, E., Froidevaux, L., Jarnot, R., Lahoz, W., Lau, C., Peckham, G., Read, W., Ricaud, P., Suttie, R., and Waters, J.: Springtime stratospheric water vapour in the southern hemisphere as measured by MLS, Geophys. Res. Lett., 20, 1235–1238, 1993. 4012

Hoogen, R., Rozanov, V. V., and Burrows, J. P.: Ozone profiles from GOME satellite data: Algorithm description and first validation, J. Geophys. Res., 104, 8263–8280, doi:10.1029/1998JD100093, 1999. 4018

Kiemle, C., Wirth, M., Fix, A., Ehret, G., Schumann, U., Gardiner, T., Schiller, C., Sitnikov, N., and Stiller, G.: First airborne water vapor lidar measurements in the tropical upper troposphere and mid-latitudes lower stratosphere: accuracy evaluation and intercomparisons with other instruments, Atmos. Chem. Phys., 8, 5245–5261, doi:10.5194/acp-8-5245-2008, 2008. 4011

Kikuchi, K., Nishibori, T., Ochiai, S., Ozeki, H., Irimajiri, Y., Kasai, Y., Koike, M., Manabe, T., Mizukoshi, K., Murayama, Y., Nagahama, T., Sano, T., Sato, R., Seta, M., Takahashi, C., Takayanagi, M., Masuko, H., Inatani, J., Suzuki, M., and Shiotani, M.: Overview and Early Results of the Superconducting Submillimeter-Wave Limb-Emission Sounder (SMILES), J. Geophys. Res., in press, 2010. 4012

Klenk, K. F., Bhartia, P. K., Kaveeshwar, V. G., McPeters, R. D., Smith, P. M., and Fleig, A. J.: Total Ozone Determination from the Backscattered Ultraviolet (BUV)Total Ozone Determination from the Backscattered Ultraviolet (BUV) Experiment Experiment, J. Appl. Meteorol., 21, 1672–1684, 1982. 4018

Kneizys, F. X., Shettle, E. P., Abreu, L. W., Chetwynd, J. H., Anderson, G. P., Gallery, W. O., Selby, J. E. A., and Clough, S. A.: Users Guide to LOWTRAN 7, Tech. rep., Air Force Geophysics Laboratory AFGL, 1986. 4024

Krecl, P., Haley, C. S., Stegman, J., Brohede, S. M., and Berthet, G.: Retrieving the vertical distribution of stratospheric OClO from Odin/OSIRIS limb-scattered sunlight measurements, Atmos. Chem. Phys., 6, 1879–1894, doi:10.5194/acp-6-1879-2006, 2006. 4029

Matthews, E.: Global Vegetation and Land Use: New High-Resolution Data Bases for Climate Studies, J. Clim. Appl. Meteorol., 22, 474–487, 1983. 4024

Milz, M., von Clarmann, T., Fischer, H., Glatthor, N., Grabowski, U., Höpfner, M., Kellmann, S., Kiefer, M., Linden, A., Mengistu Tsidu, G., Steck, T., Stiller, G. P., Funke, B., López-Puertas, M., and Koukouli, M. E.: Water vapor distributions measured with the Michelson Interferometer for Passive Atmospheric Sounding on board Envisat (MIPAS/Envisat), J. Geophys. Res., 110, D24307, doi:10.1029/2005JD005973, 2005. 4012

Nakajima, H., Sugita, T., Yokota, T., Kobayashi, H., Sasano, Y., Ishigaki, T., Mogi, Y., Araki, N., Waragai, K., Kimura, N., Iwazawa, T., Kuze, A., Tanii, J., Kawasaki, H., Horikawa, M., Togami, T., and Uemura, N.: Characteristics and performance of the Improved Limb Atmospheric Spectrometer-II (ILAS-II) on board the ADEOS-II satellite, J. Geophys. Res., 111, D11S01, doi:10.1029/2005JD006334, 2006. 4012

Nedoluha, G., Bevilacqua, R., Gomez, R., Thacker, D., Waltman, W., and Pauls, T.: Ground-based measurements of water vapor in the middle atmosphere, J. Geophys. Res., 100(D2), 2927–29399, 1995. 4011

Noël, S., Bovensmann, H., Burrows, J. P., Frerick, J., Chance, K. V., Goede, A. H. P., and Muller, C.: The SCIAMACHY Instrument on ENVISAT-1, in: Sensors, Systems, and Next-Generation Satellites II, vol. 3498 of Proc. SPIE, 94–104, 1998. 4013

Pan, L. L., Bowman, K. P., Shapiro, M., Randel, W. J., Gao, R. S., Campos, T., Davis, C., Schauffler, S., Ridley, B. A., Wei, J. C., and Barnet, C.: Chemical behavior of the tropopause observed during the Stratosphere-Troposphere Analyses of Regional Transport experiment, J. Geophys. Res., 112, D18110, doi:10.1029/2007JD008645, 2007. 4010

Pougatchev, N., August, T., Calbet, X., Hultberg, T., Oduleye, O., Schlüssel, P., Stiller, B., Germain, K. St., and Bingham, G.: IASI temperature and water vapor retrievals - error assessment and validation, Atmos. Chem. Phys., 9, 6453–6458, doi:10.5194/acp-9-6453-2009, 2009. 4012

Randel, W. J., Wu, F., Voemel, H., Nedoluha, G. E., and Forster, P.: Decreases in stratospheric water vapor after 2001: links to changes in the tropical tropopause and the Brewer-Dobson circulation, J. Geophys. Res., 111, 12312, doi:10.1029/2005JD006744, 2006. 4011

Read, W. G., Lambert, A., Bacmeister, J., Cofield, R. E., Christensen, L. E., Cuddy, D. T., Daffer, W. H., Drouin, B. J., Fetzer, E., Froidevaux, L., Fuller, R., Herman, R., Jarnot, R. F., Jiang, J. H., Jiang, Y. B., Kelly, K., Knosp, B. W., Kovalenko, L. J., Livesey, N. J., Liu, H.-C., Manney, G. L., Pickett, H. M., Pumphrey, H. C., Rosenlof, K. H., Sabounchi, X., Santee, M. L., Schwartz, M. J., Snyder, W. V., Stek, P. C., Su, H., Takacs, L. L., Thurstans, R. P., Vomel, H., Wagner, P. A., Waters, J. W., Webster, C. R., Weinstock, E. M., and Wu, D. L.: Aura Microwave Limb Sounder upper tropospheric and lower stratospheric H_2O and relative humidity with respect to ice validation, J. Geophys. Res., 112, D24S35, doi:doi:10.1029/2007JD008752, 2007. 4012

Rodgers, C. D.: Retrieval of Atmospheric Temperature and Composition From Remote Measurements of Thermal Radiation, Rev. Geophys. Space Ge., 4, 609–624, 1976. 4028

Rodgers, C. D.: Characterization and error analysis of profiles retrieved from remote sounding measurements, J. Geophys. Res., 95, 5587–5595, 1990. 4028

Rodgers, C. D.: Inverse methods for atmospheric sounding: Theory and practice, World Scientific, 2000. 4015, 4017, 4023

Rothman, L., Gordon, I., Barbe, A., Benner, D., Bernath, P., Birk, M., Boudon, V., Brown, L., Campargue, A., Champion, J.-P., Chance, K., Coudert, L., Dana, V., Devi, V., Fally, S., Flaud, J.-M., Gamache, R., Goldman, A., Jacquemart, D., Kleiner, I., Lacome, N., Lafferty, W., Mandin, J.-Y., Massie, S., Mikhailenko, S., Miller, C., Moazzen-Ahmadi, N., Naumenko, O., Nikitin, A., Orphal, J., Perevalov, V., Perrin, A., Predoi-Cross, A., Rinsland, C., Rotger, M., Simeckova, M., Smith, M., Sung, K., Tashkun, S., Tennyson, J., Toth, R., Vandaele, A., and Vander Auwera, J.: The HITRAN 2008 molecular spectroscopic database, J. Quant. Spectrosc. Ra., 110, 533–572, doi:10.1016/j.jqsrt.2009.02.013, 2009. 4024

Rozanov, A.: SCIATRAN: Radiative transfer model and retrieval software package, http://www.iup.physik.uni-bremen.de/sciatran, last access: 8 September, 2010. 4015, 4020

Rozanov, A., Rozanov, V., and Burrows, J. P.: A numerical radiative transfer model for a spherical planetary atmosphere: combined differential-integral approach involving the Picard iterative approximation, J. Quant. Spectrosc. Ra., 69, 491–512, doi:10.1016/S0022-4073(00)00100-X, 2001. 4021

Rozanov, A., Rozanov, V., Buchwitz, M., Kokhanovsky, A., and Burrows, J. P.: SCIATRAN 2.0 – A new radiative transfer model for geophysical applications in the 175–2400 nm spectral region, Adv. Space Res., 36, 1015–1019, doi:10.1016/j.asr.2005.03.012, 2005. 4015, 4020

Rozanov, V. V. and Kokhanovsky, A. A.: Impact of single- and multi-layered cloudiness on ozone vertical column retrievals using nadir observations of backscattered solar radiation, in: Light Scattering Reviews 3, edited by: Kokhanovsky, A. A., Springer, Berlin, 133–189, 2008. 4018

Rozanov, V. V. and Rozanov, A. V.: Relationship between different approaches to derive weighting functions related to atmospheric remote sensing problems, J. Quant. Spectrosc. Ra., 105, 217–242, 2007. 4021

Selkirk, H. B., Voemel, H., Valverde Canossa, J., Pfister, L., Diaz, J. A., Fernandez, W., Amador, J., Stolz, W., and Peng, G.: Detailed structure of the tropical upper troposphere and lower stratosphere as revealed by balloon sonde observations of water vapor, ozone, temperature and winds during the NASA TCSP and TC4 campaigns, J. Geophys. Res., in press, doi:10.1029/2009JD013209, 2010. 4033

AMTD
3, 4009–4057, 2010

UTLS water vapor from SCIAMACHY limb measurements

A. Rozanov et al.

Sioris, C., Zou, J., McElroy, C., McLinden, C., and Vömel, H.: High vertical resolution water vapour profiles in the upper troposphere and lower stratosphere retrieved from MAESTRO solar occultation spectra, Adv. Space Res., 46, 642–650, doi:10.1016/j.asr.2010.04.040, 2010. 4011

Sitnikov, N., Yushkov, V., Afchine, A., Korshunov, L., Astakhov, V., Ulanovskii, A., Kraemer, M., Mangold, A., Schiller, C., and Ravegnani, F.: The FLASH instrument for water vapor measurements on board the high-altitude airplane, Instrum. Exp. Tech., 50, 113–121, doi:10.1134/S0020441207010174, 2007. 4011

Sofieva, V. F., Tamminen, J., Haario, H., Kyrölä, E., and Lehtinen, M.: Ozone profile smoothness as a priori information in the inversion of limb measurements, Ann. Geophys., 22, 3411–3420, doi:10.5194/angeo-22-3411-2004, 2004. 4029

Solomon, S., Rosenlof, K. H., Portmann, R. W., Daniel, S. M. D., Sanford, T. J., and Plattner, G.-K.: Contributions of Stratospheric Water Vapor to Decadal Changes in the Rate of Global Warming, Science, 327, 1219, doi:10.1126/science.1182488, 2010. 4010

Stenke, A. and Grewe, V.: Simulation of stratospheric water vapor trends: impact on stratospheric ozone chemistry, Atmos. Chem. Phys., 5, 1257–1272, doi:10.5194/acp-5-1257-2005, 2005. 4010

Thomason, L. W., Burton, S. P., Iyer, N., Zawodny, J. M., and Anderson, J.: A revised water vapor product for the Stratospheric Aerosol and Gas (SAGE) II version 6.2 data set, J. Geophys. Res., 109, D06312, doi:10.1029/2003JD004465, 2004. 4011

Thomason, L. W., Moore, J. R., Pitts, M. C., Zawodny, J. M., and Chiou, E. W.: An evaluation of the SAGE III version 4 aerosol extinction coefficient and water vapor data products, Atmos. Chem. Phys., 10, 2159–2173, doi:10.5194/acp-10-2159-2010, 2010. 4011

Urban, J., Lautié, N., Murtagh, D., Eriksson, P., Kasai, Y., Loßow, S., Dupuy, E., de La Noë, J., Frisk, U., Olberg, M., Flochmoën, E. L., and Ricaud, P.: Global observations of middle atmospheric water vapour by the Odin satellite: An overview, Planet. Space Sci., 55, 1093–1102, doi:10.1016/j.pss.2006.11.021, 2007. 4012

Vasic, V., Feist, D., Müller, S., and Kämpfer, N.: An airborne radiometer for stratospheric water vapor measurements at 183 GHz, IEEE T. Geosci. Remote, 43, 1563–1570, doi:10.1109/TGRS.2005.846860, 2005. 4011

Vömel, H., Oltmans, S. J., Hofmann, D. J., Deshler, T., and Rosen, J. M.: The evolution of the dehydration in the Antarctic stratospheric vortex, J. Geophys. Res., 100, 13919–13926, 1995. 4032

Vömel, H., Barnes, J. E., Forno, R. N., Fujiwara, M., Hasebe, F., Iwasaki, S., Kivi, R., Komala, N., Kyrö, E., Leblanc, T., Morel, B., Ogino, S.-Y., Read, W. G., Ryan, S. C., Saraspriya, S., Selkirk, H., Shiotani, M., Valverde Canossa, J., and Whiteman, D. N.: Validation of Aura Microwave Limb Sounder water vapor by balloonborne Cryogenic Frost point Hygrometer measurements, J. Geophys. Res., 112, D24S37, doi:10.1029/2007JD008698, 2007a. 4034

Vömel, H., David, D. E., and Smith, K.: Accuracy of tropospheric and stratospheric water vapor measurements by the cryogenic frost point hygrometer: Instrumental details and observations, J. Geophys. Res., 112, D08305, doi:10.1029/2006JD007224, 2007b. 4011, 4033

Zöger, M., Afchine, A., Eicke, N., Gerhards, M.-T., Klein, E., McKenna, D. S., Mörschel, U., Schmidt, U., Tan, V., Tuitjer, F., Woyke, T., and Schiller, C.: A new family of balloon-borne and airborne Lyman photofragment fluorescence hygrometers, J. Geophys. Res., 104, 1807–1816, doi:10.1029/1998JD100025, 1999. 4011

AMTD

3, 4009–4057, 2010

UTLS water vapor from SCIAMACHY limb measurements

A. Rozanov et al.

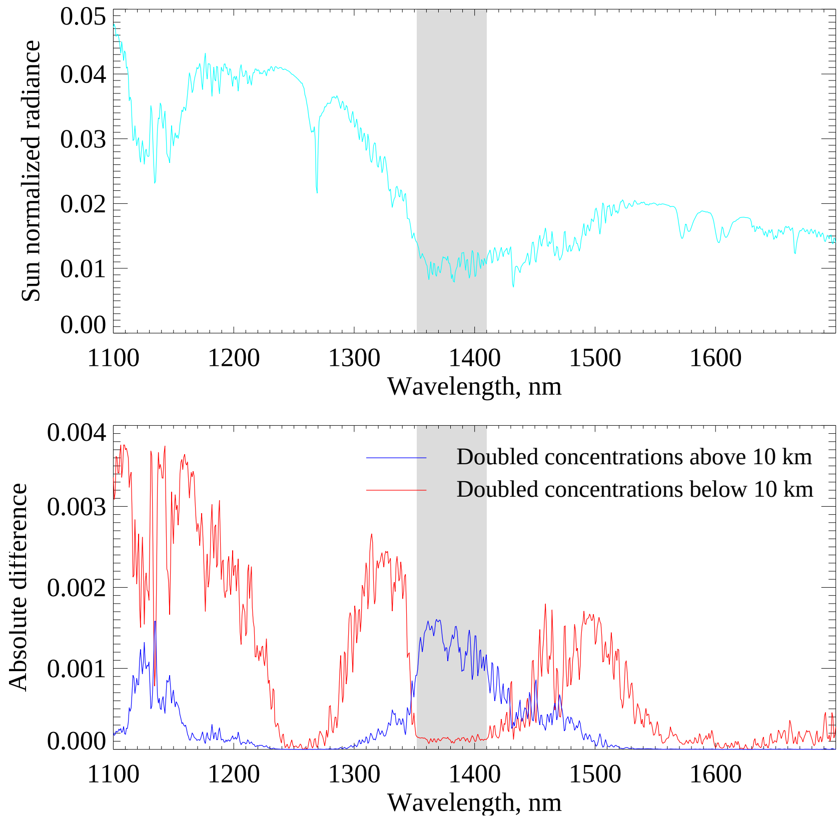

Fig. 1. Upper panel: simulated sun normalized limb radiance in spectral chanel 6 of the SCIAMACHY instrument at a tangent height of 12 km. Lower panel: Absolute differences in the simulated radiance due to doubling of water vapor amounts above (blue curve) and below (red curve) 10 km. Positive differences mean that changes in the water vapor abundance lead to a decrease in the limb radiance. Grey shaded areas mark the spectral range that is found to be optimal for the UTLS water vapor retrieval.

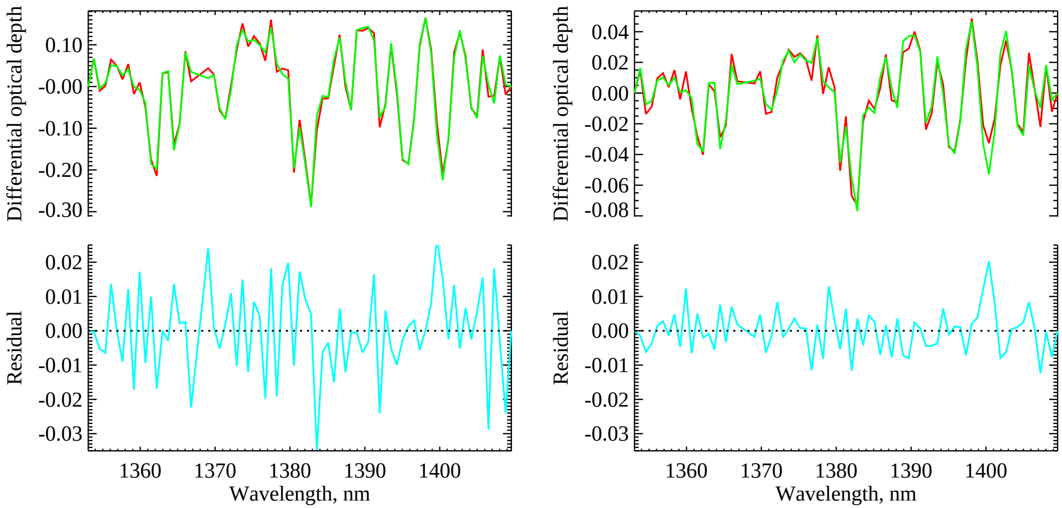

Fig. 2. Example spectral fits for tangent heights of 12 km (left panels) and 21.9 km (right panels). The upper panels show measured (red) and simulated (green) differential logarithmic spectra whereas the lower panels show fit residuals. The results are obtained for a SCIAMACHY limb measurement performed on 27 January 2004, at 17:18:22 UTC (orbit 9986) over Boulder, CO, USA (40° N,105° W).

AMTD
3, 4009–4057, 2010

Title Page
Abstract | Introduction
Conclusions | References
Tables | Figures
◄| |►
◄ ►
Back | Close
Full Screen / Esc
Printer-friendly Version
Interactive Discussion

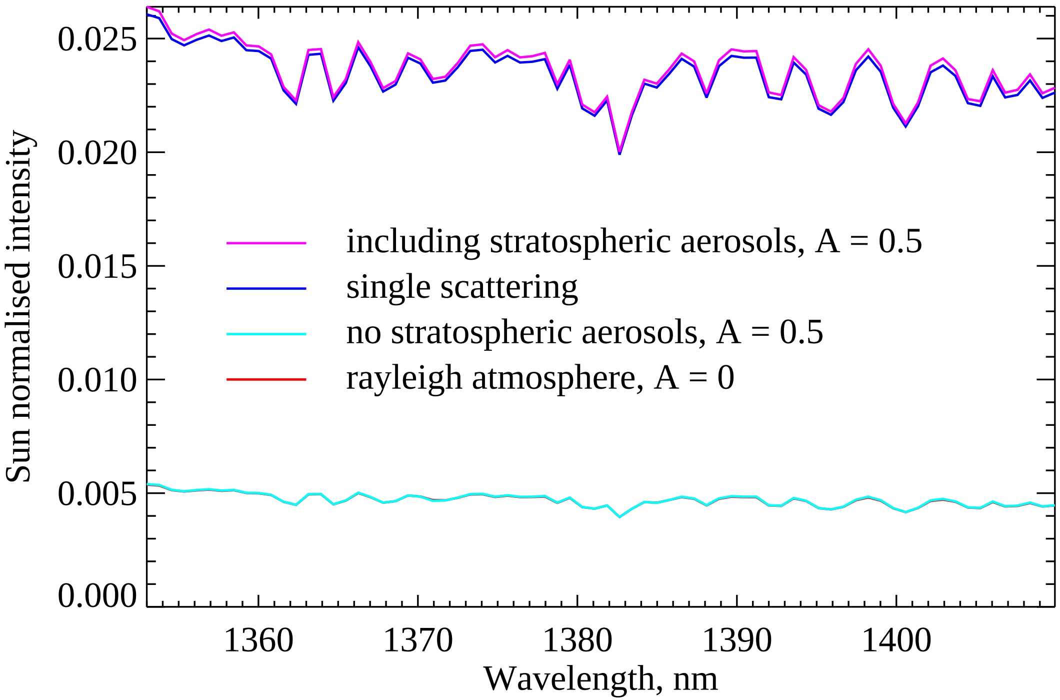

Fig. 3. Simulated limb radiance at a tangent height of 15 km and a solar zenith angle of 69° (at tangent point). Magenta line: standard simulation considering multiple scattering, background aerosols, and surface albedo of 0.5. Blue line: single scattering approximation including background aerosols. Cyan line: multiple scattering without stratospheric aerosols (above 10 km) with surface albedo set to 0.5. Red line (barely seen below the cyan line): Rayleigh scattering (including multiple scattering) with surface albedo set to 0.

AMTD
3, 4009–4057, 2010

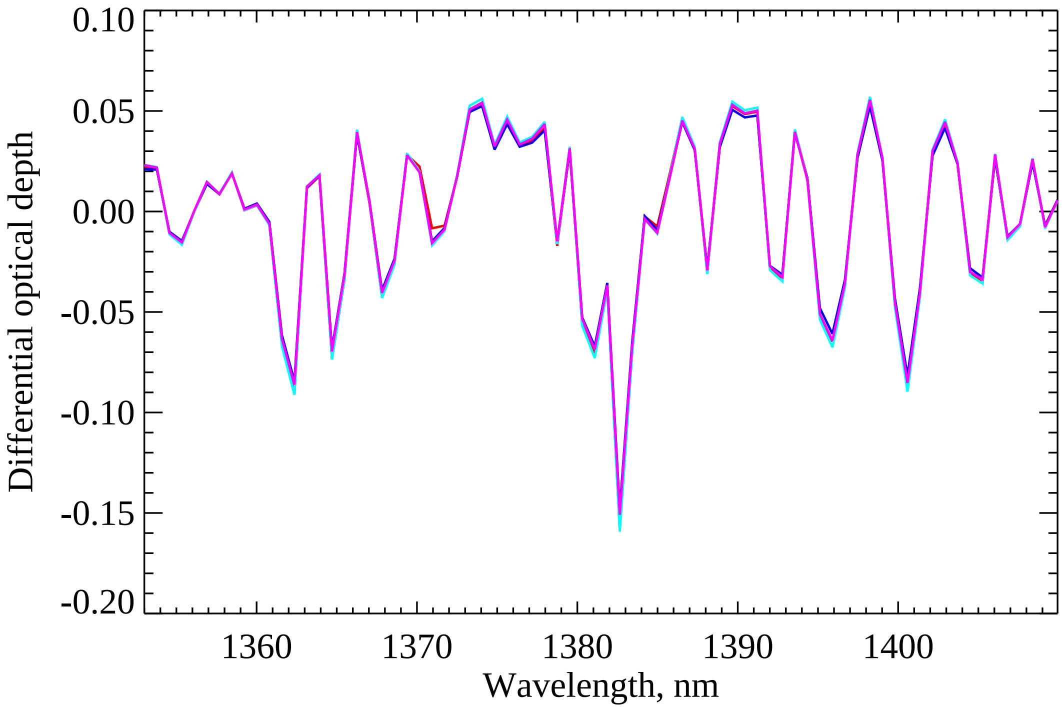

Fig. 4. Same as Fig. 3 but for differential logarithmic intensities (differential optical depths).

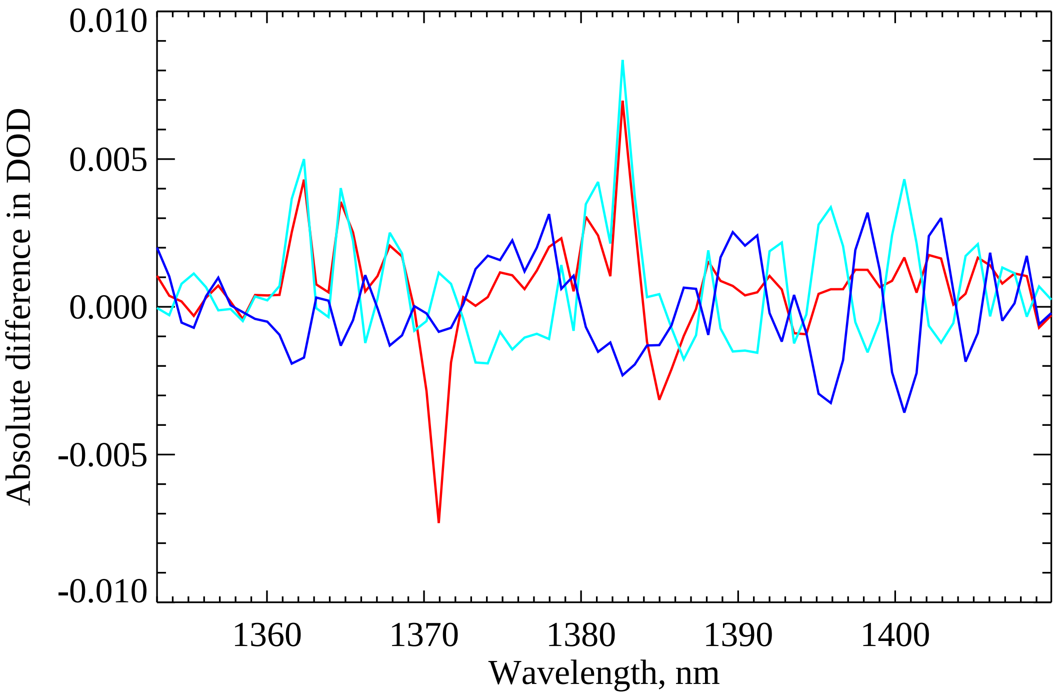

Fig. 5. Absolute differences in the differential optical depths shown in Fig. 4 with respect to the standard scenario. The color coding is the same as in Figs. 3 and 4.

AMTD
3, 4009–4057, 2010

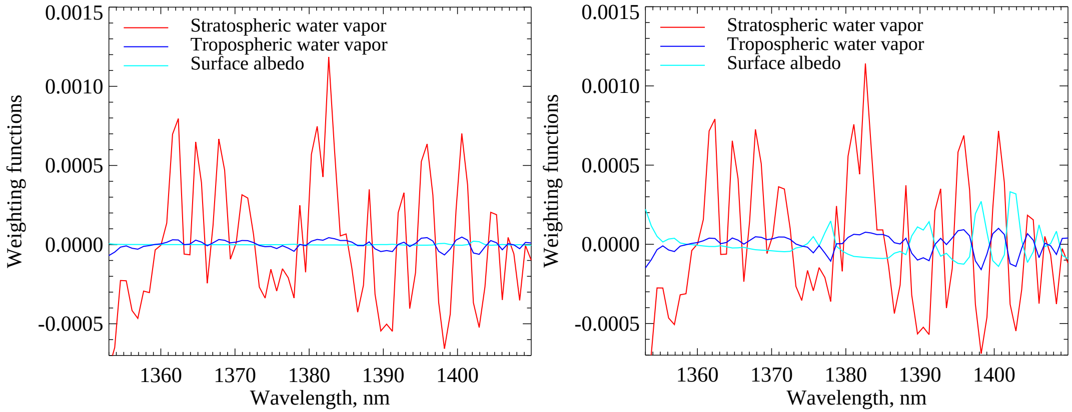

Fig. 6. Weighting functions for the stratospheric water vapor (red), tropospheric water vapor (blue), and surface albedo (cyan) for a typical SCIAMACHY limb observation (left panel) and for a surface elevation of 2 km (right panel).

AMTD
3, 4009–4057, 2010

UTLS water vapor from SCIAMACHY limb measurements

A. Rozanov et al.

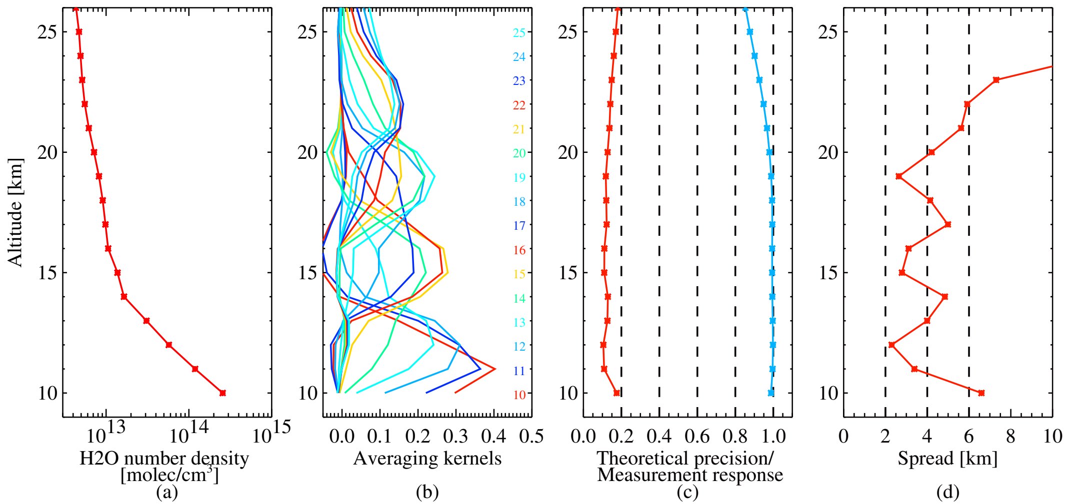

Fig. 7. Characterization of the water vapor retrieval for a typical observation in winter over Boulder, CO, USA: **(a)** vertical distribution of the water vapor number density, **(b)** averaging kernels, **(c)** theoretical precision of the retrieval (red) and measurement response function (light blue), **(d)** spread of the averaging kernels.

AMTD
3, 4009–4057, 2010

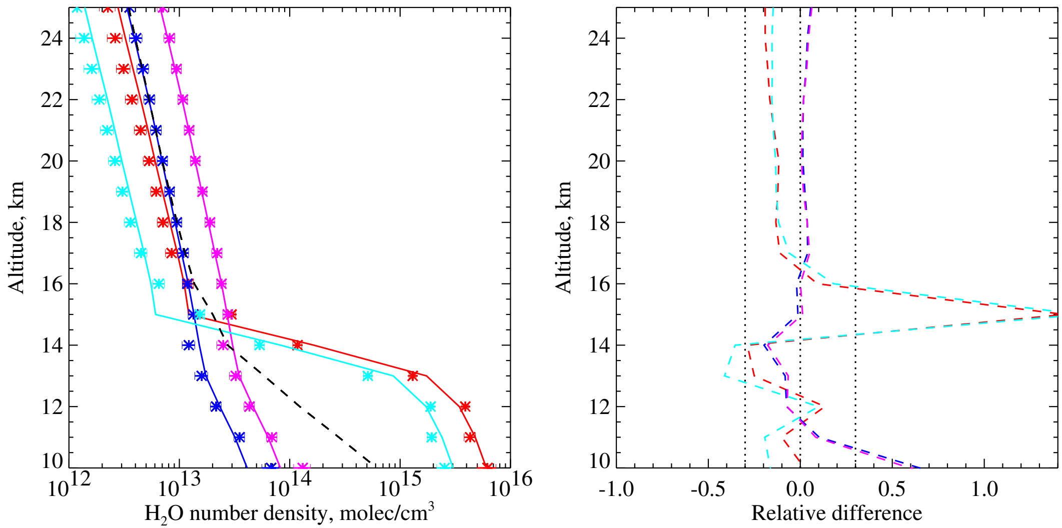

Fig. 8. Results of synthetic retrievals for different shapes of the true water vapor profile. Left panel: true (solid color lines), retrieved (asterisks), and a priori (dashed black line) water vapor profiles for different runs. Right panel: relative differences between the true and retrieved water vapor profiles.

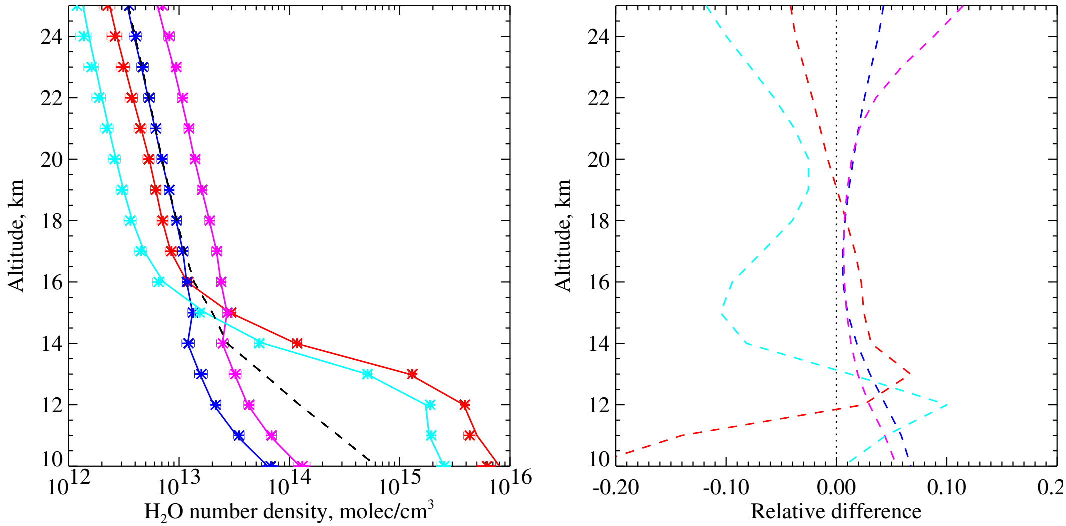

Fig. 9. Same as Fig. 8 but for the true profiles convolved with the corresponding averaging kernels.

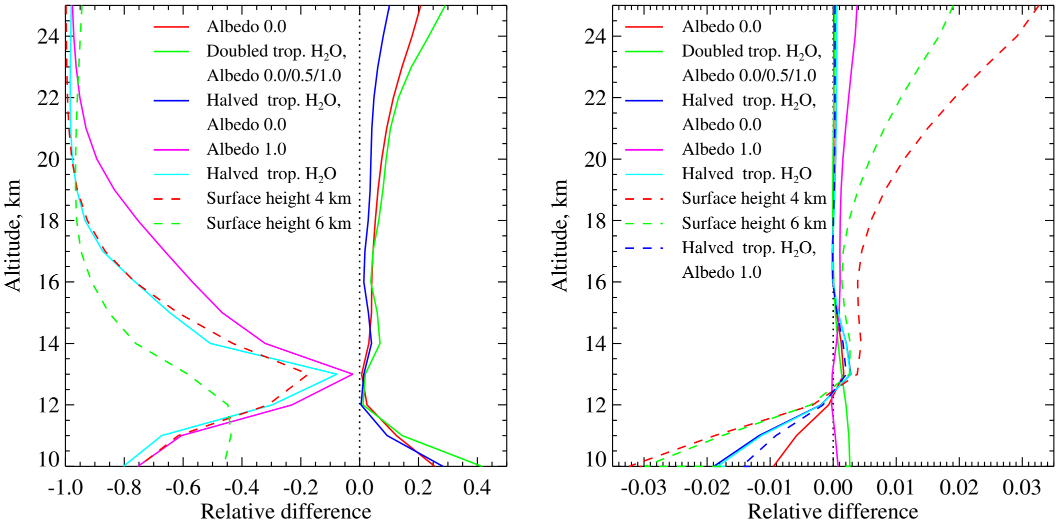

Fig. 10. Relative retrieval errors due to unknown atmospheric or surface parameters considering (right panel) and neglecting (left panel) in the retrieval process contributions of the tropospheric water vapor and of the surface albedo. See text for detailed explanations.

AMTD
3, 4009–4057, 2010

UTLS water vapor from SCIAMACHY limb measurements

A. Rozanov et al.

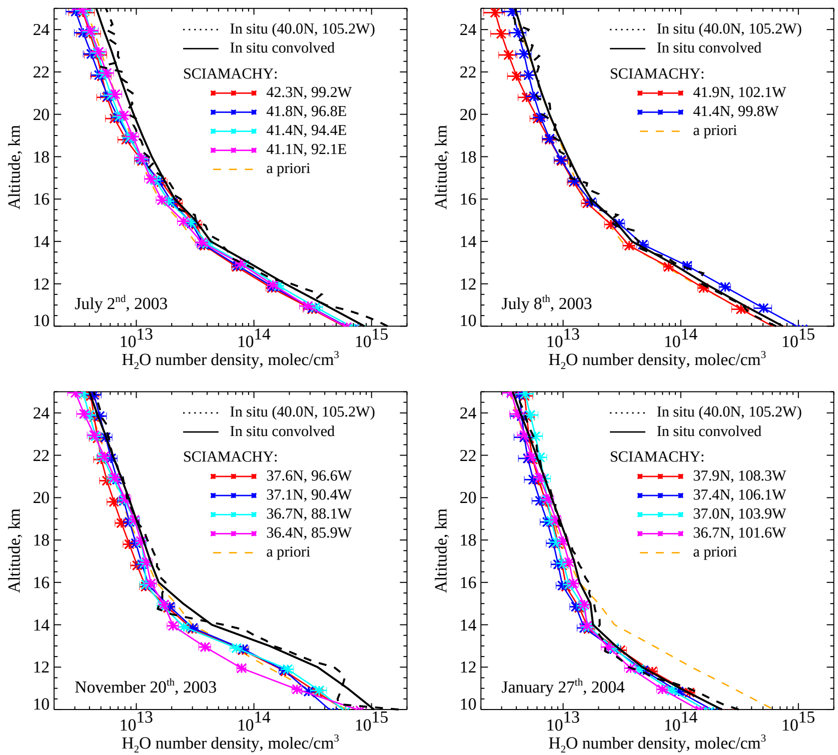

Fig. 11. Comparison to in situ measurements performed with a balloon-borne frost point hygrometer (FPH) over Boulder, CO, USA for four selected balloon launches. Original water vapor profiles obtained from the frost point hygrometer are shown with black dashed lines whereas black solid lines show the same profiles but convolved with SCIAMACHY averaging kernels. Color solid lines depict water vapor profiles retrieved from SCIAMACHY limb observations (up to four profiles per limb observation due to an azimuthal scan) and the dashed orange line shows the a priori water vapor profile used for SCIAMACHY retrievals.

AMTD
3, 4009–4057, 2010

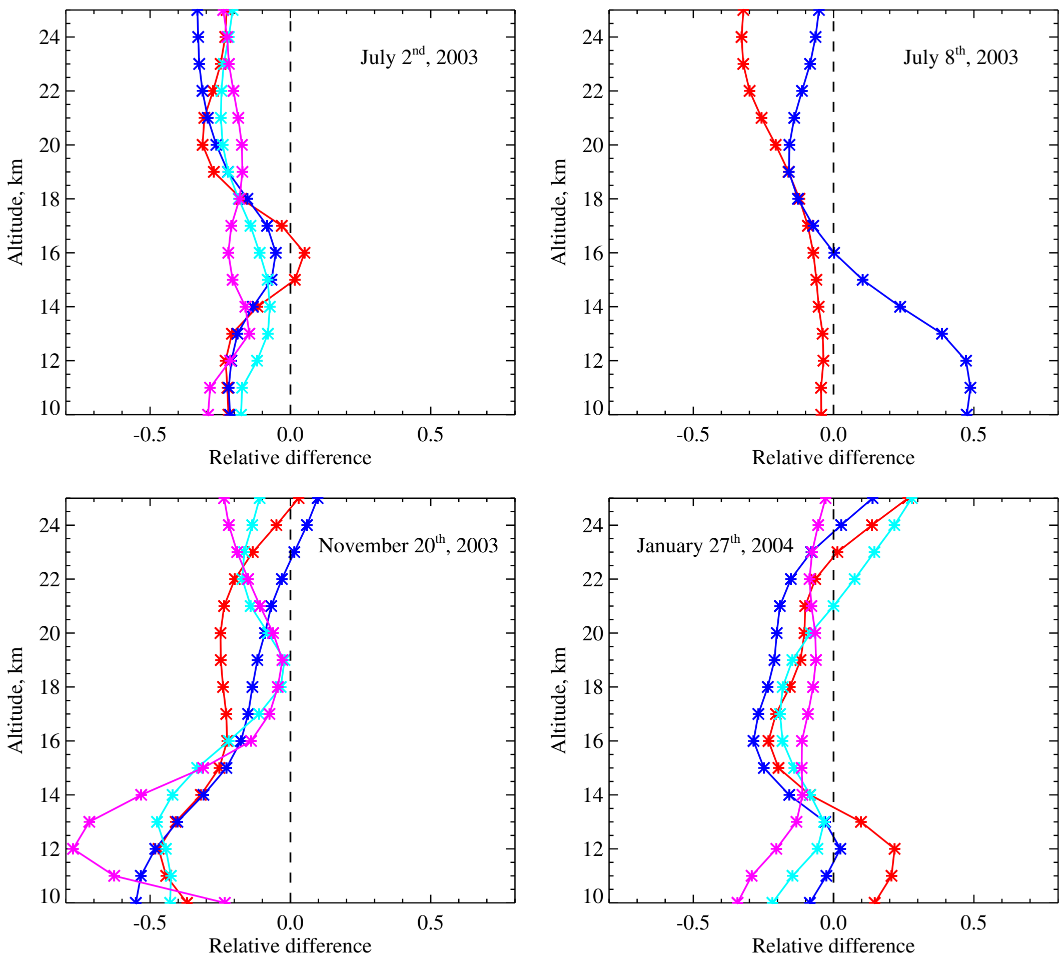

Fig. 12. Same as Fig. 11 but for relative differences.

AMTD

3, 4009–4057, 2010

UTLS water vapor from SCIAMACHY limb measurements

A. Rozanov et al.

Title Page
Abstract | Introduction
Conclusions | References
Tables | Figures
◀| |▶
◀ ▶
Back | Close
Full Screen / Esc
Printer-friendly Version
Interactive Discussion

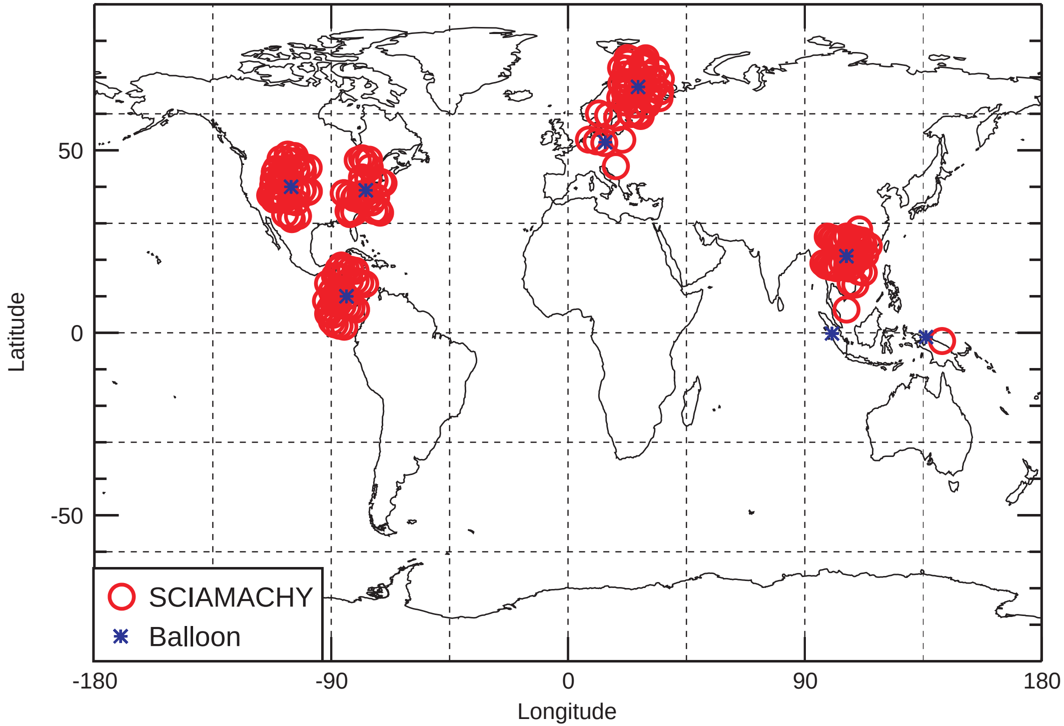

Fig. 13. Locations of balloon launch sites considered in this study and tangent points of coinciding SCIAMACHY observations.

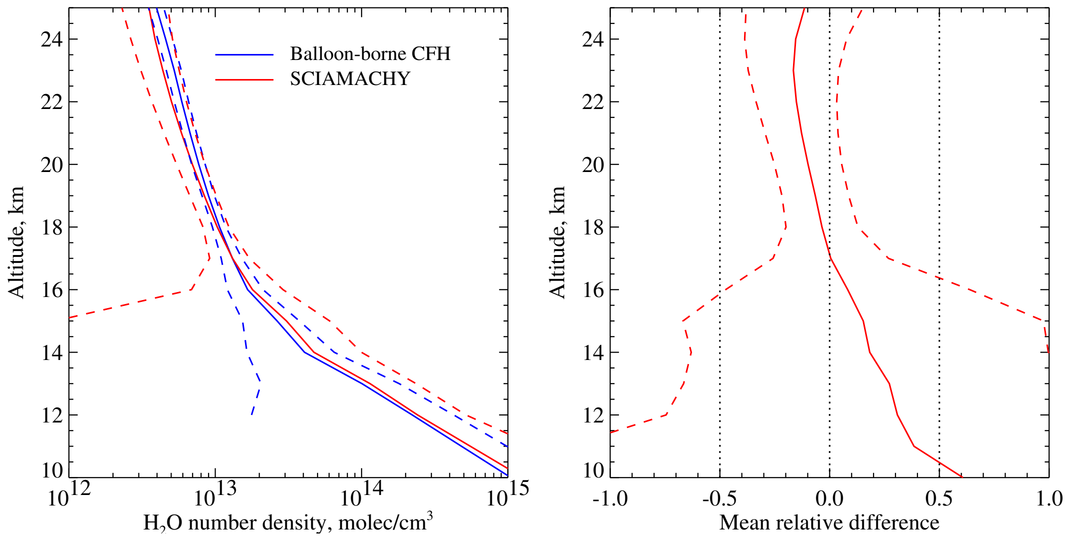

Fig. 14. Comparison to in situ balloon-borne observations. Left panel: solid lines show balloon-borne CFH (blue) and SCIAMACHY (red) profiles averaged over all balloon launches at all locations as shown in Fig. 13 whereas dashed lines depict corresponding standard deviations. Right panel: mean relative difference between SCIAMACHY and balloon-borne CFH results (solid line) and corresponding standard deviation (dashed lines).

AMTD
3, 4009–4057, 2010

UTLS water vapor from SCIAMACHY limb measurements

A. Rozanov et al.

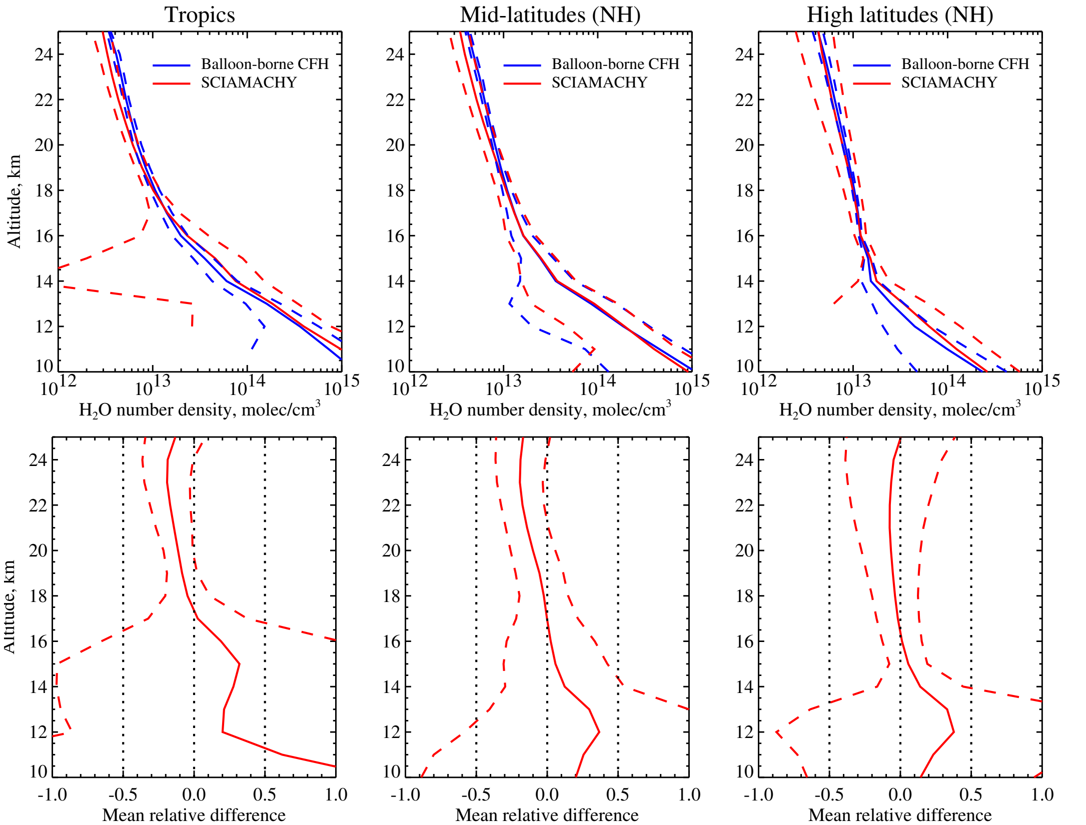

Fig. 15. Comparison to in situ balloon-borne observations for different latitudinal ranges: tropics (left), mid-latitudes of the Northern Hemisphere (middle), and high latitudes of the Northern Hemisphere (right). Upper panels show average balloon-borne CFH (blue) and SCIAMACHY (red) profiles with solid lines and corresponding standard deviations with dashed lines. Lower panels show mean relative differences between SCIAMACHY and balloon-borne CFH results (solid line) and corresponding standard deviations (dashed lines).

AMTD
3, 4009–4057, 2010

UTLS water vapor from SCIAMACHY limb measurements

A. Rozanov et al.